Growth mechanism of interfacial fluid-mixing width induced by successive nonlinear wave interactions

Haifeng Li [1], Baolin Tian,[1,2,*] Zhiwei He,[1] and Yousheng Zhang [1,2,†]

[1]*Institute of Applied Physics and Computational Mathematics, Beijing 100094, China*
[2]*HEDPS, Center for Applied Physics and Technology, and College of Engineering, Peking University, Beijing 100871, China*

Interfacial fluid mixing induced by successive waves, such as shock, rarefaction, and compression waves, plays a fundamental role in engineering applications, e.g., inertial confinement fusion, and in natural phenomena, e.g., supernova explosion. These waves bring nonuniform, unsteady external forces into the mixing zone, which leads to a complex mixing process. The growth rate of the mixing width is analyzed by decomposing the turbulent flow field into the averaged field and the fluctuating counterpart. The growth rate is thus divided into three parts: (i) the stretching or compression (S(C)) effect induced by the averaged-velocity difference between two ends of the mixing zone, (ii) the penetration effect induced by the fluctuations which represent the penetration of the two species into each other, and (iii) the diffusive effect, which is induced by the molecular diffusion and is negligible in high-Reynolds-number flows at Schmidt number of order unity. The penetration effect is further divided into the Richtmyer-Meshkov (RM) effect, which is induced by fluctuations that were deposited by earlier wave interactions, and the Rayleigh-Taylor (RT) effect, which is caused by the fluctuations that arise in an overall acceleration of the mixing zone. During the passage of the rarefaction waves, the mixing zone is stretched, while during the passage of the compression waves or shock waves, the mixing zone is compressed. To illustrate these effects, a physical model of RM mixing with reshock is used. By combining the S(C), RM, and RT effects, the entire evolution of mixing width is restructured, which agrees well with numerical simulations for problems with a wide range of density ratios.

I. INTRODUCTION

Interfacial fluid mixing occurs when an irregularly perturbed interface separating two fluids with different densities (ρ_h and ρ_l for heavy and light fluids, respectively) is subjected to an external force directing from the light fluid to the heavy fluid or an impulsive acceleration, which are known as the Rayleigh-Taylor (RT) mixing [1,2] and the Richtmyer-Meshkov (RM) mixing [3,4], respectively. The fluids penetrate into each other, giving rise to a mixing zone that consists of a bubble zone (the structures where the light fluid penetrates into the heavy fluid) and a spike zone (the structures where the heavy fluid penetrates into the light fluid). As a primary quantity describing the evolution of the mixing zone [5], the mixing width ($h(t)$, defined as the distance from the bubble-zone front to the spike-zone front) plays a fundamental role in engineering applications such as inertial confinement fusion [6,7] and in natural phenomena such as supernova explosion [8].

Generally, the evolution of the mixing zone depends on the initial flow field of the mixing zone at t_0, denoted as $\Phi(t_0)$, and the external forces that change with the spatial coordinate **x** and time t, denoted as $\mathcal{F}(\mathbf{x}, t)$. The well-known RT mixing

and the RM mixing are two classical representatives of the general interfacial fluid mixing.

For classical RT mixing, the initial flow field is steady and the perturbations at the interface grow because of the external force [which results in an acceleration $g(t)$ of the system]. The RT mixing with a constant acceleration $g(t) = g_0$ has been investigated widely [9–11]. In the late stage, the flow achieves a self-similar state; the spike and/or bubble width is given by $h_i = \alpha_i A g_0 (t + t_{i,0})^2$, where $i = s, b$ denotes the spike and the bubble, with A being the Atwood number, defined as $A = (\rho_h - \rho_l)/(\rho_h + \rho_l)$. For α_b, its observed value has changed widely from 0.02 to 0.12, which is mainly determined by the initial perturbations and correspondingly the different evolution mechanisms (merging and competition of the bubbles) [12–18]. Besides, as the density ratio ρ_h/ρ_l increases, α_s increases as well. The dependence of α_s on the density ratio is still under investigation [19]. For RT mixing driven by variable acceleration, two kinds of length, $\Omega = 0.5(\int \sqrt{g}dt)^2$ and $\Xi = \iint gdt'dt$ are proposed to scale the evolution of the turbulent mixing width [20–22].

For classical RM mixing, the external force is loaded instantaneously at t_0 (more precisely, it happens in a timescale that is much smaller than the timescale during which the RM mixing develops). The mixing zone is compressed by the shock wave [3], and the basic flow variables (density, pressure, velocity, and temperature) are perturbed [23], which forms the initial condition of RM mixing, i.e., $\Phi(t_0^+)$. Therefore, $\Phi(t_0^+)$ determines the following evolution of the mixing width. To

---
*tian_baolin@iapcm.ac.cn
†zhang_yousheng@iapcm.ac.cn

be specific, the mixing zone undergoes a startup process [24], a linear-growth phase [3,4,25], and then a power-law-growth phase with the width $h(t) \propto t^\theta$, where θ represents a power index of the classical RM turbulent mixing [26–31]. The power-law growth indicates a decaying of the initial energy (mainly the initial vorticity deposited by the shock wave). The values of θ change from case to case (smaller than 2/3) [28]. Inogamov and Oparin [28,29] gave the values of θ as 2/5 for the two-dimensional RM turbulence and $1/3 = 0.33$ for the three-dimensional one. Thornber *et al.* [32] inspected the influence of different three-dimensional multi-mode initial conditions on the turbulent mixing induced by the RM instability. Simulations with the narrow-band initial condition gives a power-law exponent $\theta \approx 0.26$ at an Atwood number of 0.5 and $\theta \approx 0.30$ at an Atwood number of 0.9. The broadband case using a perturbation power spectrum of the form $P(k) \propto k^{-2}$ gives a power-law exponent $\theta = 0.62$.

However, the actual problems generally involve complex external forces that change with the spatial position **x** and time t. Examples involve successive nonlinear waves, i.e., shock waves, rarefaction waves, and compression waves, which have been widely observed in real conditions. During the interaction of an individual wave with the mixing zone, the initial flow field is the turbulent field inherited from the earlier stages. Meanwhile, the mixing zone is accelerated by the waves partially or as a whole object. That is to say, both the initial flow field $\Phi(t_0)$ and the successive external force $\mathcal{F}(\mathbf{x}, t)$ contribute to the evolution of mixing zone. The fluid mixing under such complex conditions has practical meanings for engineering applications.

One typical physical model to study the interfacial fluid mixing induced by the successive waves is the RM mixing with reshock, which has been widely investigated over the past decades. In one situation, the initial shock propagates from the light fluid to the heavy fluid [33–41]. In this case, the interface is initially accelerated by a shock wave and then the transmitted shock reflects to accelerate the mixing zone for a second time. After that, the mixing zone is influenced by the rarefaction and compression waves alternatively [36,41]. For the first two periods after the passage of the shock waves, the evolution can be described with the analytical model considering the RM effect [30]. For the linear growth behavior immediately after reshock, i.e., $h = h_0 + 2\alpha A \Delta V t$, many numerical and experimental studies have been carried out to determine the linear growth rate after reshock [33,35,36,42–44]. Using both experiments and numerical simulations at a post-reshock Atwood number of 0.712, Leinov *et al.* [35] obtained α values ranging from 0.14 to 0.195. For a single-mode configuration, Bouzgarrou *et al.* [45] obtained a larger value. Based on the impulsive growth of a slightly perturbed diffuse interface and an empirical closure, Lombardini *et al.* [36] obtained a model that shows an A^2 dependence of the reshock growth rate in the range of small and moderate Atwood ratios. Thornber *et al.* [42] extended the theory of Mikaelian [46] to account for the molecular mixing in the mixing zone prior to reshock. In another situation, the initial shock propagates from the heavy fluid to the light fluid [47,48] and the mixing zone is decelerated by several reflected shock waves with decreasing strength.

When the waves (especially rarefaction and compression waves in the late stage) interact with the mixing zone, what are the mechanisms controlling the mixing-width evolution? Hill *et al.* [34] suggested that the decreasing in growth rate during the compression wave is because of the saturation in turbulent motions. In a recent paper by Mikaelian [30], the RT instability is believed to contribute to the mixing-width growth. For the interaction between a single-mode perturbation with a pure rarefaction wave, Morgan *et al.* [49,50] and Liang *et al.* [51] treated it as a variable-acceleration RT problem. However, as will be shown, these effects are not enough to describe the entire evolution of mixing width up to the late stage. In the present work, the flow field is decomposed into the mean field and the fluctuation field, namely Reynolds decomposition [52] and Favre decomposition [53]. The turbulent mixing is investigated considering the contribution of the mean flow field and the fluctuation counterpart. Results show that the growth rate of the mixing width includes threes parts: (i) the stretching or compression (S(C)) effect induced by mean-velocity difference between two ends of the mixing zone during the propagation of waves, (ii) the penetration effect induced by the fluctuation field which represents the penetration of the species into each other, and (iii) the diffusive effect which denotes the molecular diffusion. The diffusion effect is negligible in high-Reynolds-number flows at Schimdt number of order unity. Furthermore, it is proposed that the penetration effect can be divided into the RM effect, which represents the influence of the initial fluctuation field [10], and RT effect, which represents the fluctuation field induced by the in-process external forces. Finally, the S(C), RM, and RT effects are combined to establish an analytical model, which is able to describe the evolution of the mixing width up to the very late stage in problems with a wide range of density ratios.

Numerical simulations are used to illustrate the physical process and to evaluate the proposed model. The paper is organized as follows. The governing equations, the numerical schemes, the computational configurations, and the physical process of RM mixing with reshock are described in Sec. II. The theoretical basis and discussions of the effects are given in Sec. III. An analytical model by combining the S, C, RM and RT effects are proposed and validated with numerical simulations in Sec. IV. A summary is given in Sec. V.

II. COMPUTATIONAL CONFIGURATIONS AND PROBLEM DESCRIPTION

A. Governing equations and numerical method

The flow field can be described by the three-dimensional multicomponent Navier-Stokes equations and mass-fraction equations as follows:

$$\frac{\partial \rho}{\partial t} + \nabla \cdot (\rho \boldsymbol{u}) = 0, \tag{1a}$$

$$\frac{\partial \rho \boldsymbol{u}}{\partial t} + \nabla \cdot (\rho \boldsymbol{uu} + p\boldsymbol{\delta} - \boldsymbol{\tau}) = 0, \tag{1b}$$

$$\frac{\partial \rho E}{\partial t} + \nabla \cdot [(\rho E + p)\boldsymbol{u}]$$
$$- \nabla \cdot (\boldsymbol{\tau} \cdot \boldsymbol{u} - \boldsymbol{q}_c - \boldsymbol{q}_d) = 0, \tag{1c}$$

$$\frac{\partial \rho Y_m}{\partial t} + \nabla \cdot (\rho \boldsymbol{u} Y_m) + \nabla \cdot \boldsymbol{J}_m = 0, \tag{1d}$$

$$f = f(\rho, T, Y_m), \quad f = p, e, C_v, C_p, C_s, \ldots. \tag{1e}$$

In Eq. (1), $\boldsymbol{u} = [u, v, w] = [u_1, u_2, u_3]$ denotes the velocity vector, t is time, ρ is density, p is pressure, and E is the total energy. Y_m is the mass fraction of the species $m = 1, 2, \ldots, M$, with M being the total number of the species, satisfying $\sum_{m=1}^{M} Y_m = 1$. In the present cases, $M = 2$. $\boldsymbol{\delta}$ is the Kronecker function. The coordinates in three directions are $[x, y, z]$ or $[x_1, x_2, x_3]$. The viscous stress tensor

$$\boldsymbol{\tau} = 2\mu \left[\boldsymbol{S} - \frac{1}{3}(\nabla \cdot \boldsymbol{u})\boldsymbol{\delta} \right], \tag{2}$$

in which μ is the mixture viscosity, $\boldsymbol{S}$ is the strain-rate tensor, and its components are defined as $S_{ij} = (\partial u_i/\partial x_j + \partial u_j/\partial x_i)/2$, where $i, j = 1, 2, 3$. Based on the Fourier's law, the heat flux is defined as

$$\boldsymbol{q}_c = -\nabla \cdot (\kappa T), \tag{3}$$

with T being the temperature. The interspecies-diffusion heat flux is

$$\boldsymbol{q}_d = \sum_{m=1}^{M} C_{pm} T \boldsymbol{J}_m, \tag{4}$$

with

$$\boldsymbol{J}_m \approx -D\rho \nabla Y_m. \tag{5}$$

Here, D is the mixture diffusion coefficient and C_{pm} is the constant-pressure specific heat of species m. The equation of state for an ideal gas is applied to close the equations, i.e.,

$$\rho e = p/(\gamma - 1), \tag{6}$$

with $\gamma = C_p/C_v$, the specific heat ratio of the mixture, and e is the internal energy so that

$$E = e + \mathbf{u} \cdot \mathbf{u}/2. \tag{7}$$

The thermodynamic quantities of the mixture are modeled with the isothermal and partial pressure assumptions as in Ref. [54]. To be specific, the density and the pressure of the mixture are obtained by the addition of the physical variables of each species. The volume and temperature are equal for each species, while the physical-property parameters, such as specific heat at constant volume, are obtained by a linear addition weighted with the mass fractions:

$$f = \sum_{m=1}^{M} f_m \quad \text{for } f = \rho, p,$$

$$f = f_1 = \cdots = f_M \quad \text{for } f = T, V,$$

$$f = \sum_{m=1}^{M} Y_m f_m \quad \text{for } f = \mu, \kappa, D, C_p, C_v. \tag{8}$$

For the mth species, the Sutherland viscosity law [55] is applied to calculate the viscosity,

$$\mu_m = \mu_{0,m} \left(\frac{T}{T_0} \right)^{3/2} \frac{T_0 + T_s}{T + T_s}, \tag{9}$$

TABLE I. Physical properties of the gases. SF_6 is actually a mixture of SF_6 and acetone (Ac) with the mass fractions of 0.8 and 0.2, respectively [39].

Quantity	M [kg kmol^{-1}]	γ	μ_0 [kg m^{-1} s^{-1}]	Pr	Sc
H_2	2.02	1.41	0.8287×10^{-5}	0.69	1.79
Air	28.83	1.40	1.7161×10^{-5}	0.72	0.76
CO_2	44.01	1.29	1.3922×10^{-5}	0.76	0.51
SF_6	112.10	1.10	1.2388×10^{-5}	0.80	0.69

with $\mu_{0,m}$ being a reference viscosity at a reference temperature T_0. In the present work, $T_0 = 273.15$ K is used and the reference viscosity of the species are listed in Table I. T_s is an effective temperature, which changes among different substances [55], and $T_s = 124$ K is applied to approximately calculate the viscosity at moderate temperature and pressures.

The thermal conductivity κ_m and diffusivity D_m of the mth species are the same as those in Ref. [36], which are calculated as

$$\kappa_m = C_{p,m} \frac{\mu_m}{\text{Pr}_m}, \tag{10}$$

$$D_m = \frac{\mu_m}{\rho_m \text{Sc}_m}, \tag{11}$$

The Prandtl number Pr_m and Schmidt number Sc_m for the species are listed in Table I.

The numerical simulation is implemented in the code of finite difference for compressible fluid dynamics (CFD^2), which has been validated in our previous paper [41] and has been used to investigate the RT instability [56–58] and RM instability [59]. For the convective term, an improved fifth-order monotonicity-preserving scheme (MP-R) [60–62] with a Riemann solver proposed by Harten, Lax, and Van Leer (HLL) is used. The temporal integration marches with a third-order Runge-Kutta scheme.

B. Computational configurations

The problem considered is illustrated in Fig. 1, which includes a shock tube with an end wall. A shock wave initially propagates from gas 1 to gas 2 and reflects off the end wall. The cases are designed for two purposes. The first purpose is to show the influence of the shock, rarefaction, and compression waves on the evolution of mixing zone. The initial density of gas 1 is lighter than that of gas 2. Thus, the initial shock wave travels from the light gas to the heavy gas and the initial Atwood number is positive. Three cases with the initial density ratios ρ_h/ρ_l of 1.52, 3.89, and 14.4 are presented; the corresponding light- and heavy-gas combinations are (air, CO_2), (air, SF_6), and (H_2, air), which are referred to as air-CO_2, air-SF_6, and H_2-air, respectively. For the second purpose, one more case with an initial negative Atwood number is simulated. The gas 1 and gas 2 combination is (SF_6, air), which is named SF_6-air. In comparison with the case air-SF_6, the distinguishing feature of the mixing-zone evolution when the initial shock wave travels from the heavy fluid to light fluid is given.

The shock wave with an initial Mach number Ma $= 1.5$ propagates in the positive x direction. The spanwise directions
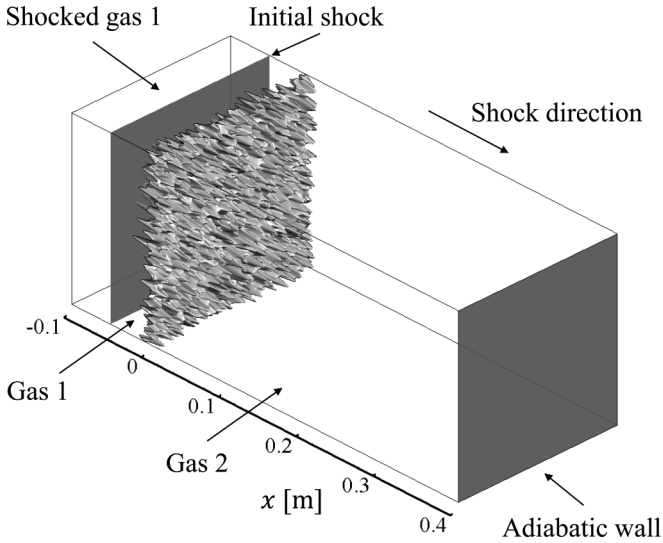
FIG. 1. A sketch of the computational domain and initial conditions in RM mixing with reshock.

are denoted as y and z. The computational domain of all the cases are given in Table II. The core area of the computational domain starts from $x_{\min} = -0.5L_0$ to $x_{\max} = 2L_0$, with $L_0 = 0.2$ m. The shock wave is initialized at $x = -0.25L_0$. In the region $x < -0.5L_0$, a buffer region is used, which is long enough to avoid shock reflections at the outflow boundary. To save computational cost, the buffer region is discretized with stretched grids. A nonreflection boundary condition is imposed at the start of the buffer region. At the boundaries normal to the y and the z directions, a periodic boundary condition is used. At the end of the tube, i.e., $x = 2L_0$, an adiabatic wall boundary is applied. The computational domains and grid numbers of the core region for all the cases are given in Table II.

The preshock state is initially set with the stagnation condition being $p_0 = 23\,000$ Pa and $T_0 = 298$ K. The pre- and postshock states satisfy the Rankine-Hugoniot conditions. Other properties of the initial gases are listed in Table III.

The initial perturbations of the material interface are set using an inverse-Fourier method, as in Ref. [31], which uses a power spectrum with constant energy at all initialized wavelengths. The initial scales in the perturbation range from $\lambda_{\min} = L_0/32$ to $\lambda_{\max} = L_0/8$, with the root mean square of the perturbations being $\lambda_{\min}$. The amplitude and phase of each mode are computed from a Gaussian distribution of deterministic random numbers with the mean amplitude satisfying the specified power spectrum; see Appendix A for details. A diffuse initial interface of error function is imposed to compute

the mole fraction of gas 1 as

$$X_1(x, y, z) = \frac{1}{2}\mathrm{erfc}\left(\frac{\sqrt{\pi}[x - \eta(y, z)]}{\delta}\right), \quad (12)$$

where $\delta = 0.05L_0$, $\eta(y, z)$ is the perturbation satisfying the specified power spectrum, and $X_2 = 1 - X_1$ represents the mole fraction of the gas 2. The interface is thus initialized at $x - \eta(y, z) = 0$. To improve the quality of the initial perturbations on coarse meshes, the initial mole fraction is evaluated in $4 \times 4 \times 4$ subcells for each computational cell and then summed to give the mole fraction for each computational cell. The mole fractions are then transferred to mass fractions to be used in numerical simulations as

$$Y_\alpha = \frac{X_\alpha M_\alpha}{\sum_i X_i M_i}, \quad (13)$$

where M_i is the molecular weight of the ith species, which is given in Table I. A visualization of the isosurface with $Y_1 = 0.5$ is given in Fig. 1.

The method of initializing the perturbations is validated using the θ-group case [31]. This case is a RM mixing with multimode initial perturbations, which has been simulated with eight independent codes. The results obtained with the present code agree well with code-averaged results (see Appendix B). This comparison validates the present code as well.

The importance of the molecular viscosity can be estimated using the Reynolds number, which can be defined as $\mathrm{Re} \equiv h\dot{h}/(\mu/\rho)$, where h is the width of the mixing zone [Eq. (17)] and $\dot{h}$ is its growth rate [Eq. (19)]. Using the numerical data (e.g., the results of the case air-SF$_6$ in Sec. II C), h is in the range from 0.02 to 0.1 m and $\dot{h}$ is in the range from 20 to 100 m s^{-1}. From Tables I and III, $\mu \approx 1 \times 10^{-5}$ kg m^{-1} s^{-1} and $\rho \approx 1$ kg m^{-3}. Therefore, Re ranges from 4×10^4 to 1×10^6 and the mixing zone is in the high-Reynolds-number regime in most of the duration of the simulation. Besides, the Prandtl number and Schmidt number are of order unity (Table I). The estimates indicate that the effects of the molecular viscosity, heat conduction, and diffusion on the evolution of the large-scale structures are negligible.

In simulations of turbulent mixing at high Reynolds number, there are generally two methods. In the first method, the Eulerian equations are solved, which is called the implicit large-eddy simulation (ILES) since the implicit numerical dissipation serves as the subgrid dissipation [18]. In the second method, the Navier-Stokes equations are solved, in which the viscosity, the molecular diffusion, and the thermal conduction are included, e.g., Ref. [39]. In both methods, a grid-convergence study is necessary to ensure that the results given in the paper are reliable. In the present work, the second method is chosen and a grid-convergence study is carried out.

TABLE II. Computational domains, grid numbers, and spectrum of the initial perturbations for the numerical cases presented in this paper.

Cases	Computational domain	Grid numbers	Perturbation spectrum
Air-CO$_2$	$[-0.5L_0, 2L_0] \times [0, L_0] \times [0, L_0]$	$960 \times 375 \times 375$	$P(k) \sim k^0$, $k \in [16\pi/L_0, 64\pi/L_0]$
Air-SF$_6$			
H$_2$-air	$[-0.5L_0, 2L_0] \times [0, 2L_0] \times [0, 2L_0]$	$960 \times 750 \times 750$	
SF$_6$-air	$[-0.5L_0, 2L_0] \times [0, L_0] \times [0, L_0]$	$960 \times 375 \times 375$	

TABLE III. Initial properties of pure light and heavy gases. ρ, U, p, T, and c_0 denote the density, velocity, pressure, temperature, and sound speed of the gases, respectively.

	Quantity	ρ [kg m^{-3}]	U [m s^{-1}]	p [Pa]	T [K]	c_0 [m s^{-1}]
Air-CO$_2$	Postshock light gas	0.498	240.8	56541	393.4	398.5
	Preshock light gas	0.268	0.0	23000	298.0	346.9
	Preshock heavy gas	0.408	0.0	23000	298.0	269.5
Air-SF$_6$	Postshock light gas	0.498	240.8	56541	393.4	398.5
	Preshock light gas	0.268	0.0	23000	298.0	346.9
	Preshock heavy gas	1.040	0.0	23000	298.0	155.9
H$_2$-air	Postshock light gas	0.035	909.1	56641	395.2	1514.4
	Preshock light gas	0.019	0.0	23000	298.0	1315.1
	Preshock heavy gas	0.268	0.0	23000	298.0	346.9
SF$_6$-air	Postshock heavy gas	2.214	123.6	53119	323.5	162.4
	Preshock heavy gas	1.040	0.0	23000	298.0	155.9
	Preshock light gas	0.268	0.0	23000	298.0	346.9

The results show that a grid resolution of 5.3×10^{-4} m, i.e., about 12 grid nodes per λ_{min}, in the spanwise direction can give converged results in terms of the mixing width. Therefore, the resolution is used for the cases listed in Table II. See Appendix C for details.

In the postprocessing of the numerical data, plane average is used to obtain the averaged properties of the flow field; i.e., the variable f is decomposed into the plane-averaged quantity and the fluctuating part, i.e., Reynolds decomposition [52] $f = \bar{f} + f'$, where $\bar{f}(x) = \iint_\Psi f(x, y, z)dydz/A_c$ and the cross area $A_c = \iint_\Psi dydz$. Ψ refers to the cross section at a streamwise location x. The Favre decomposition is denoted by $f = \tilde{f} + f''$, where $\tilde{f} = \overline{\rho f}/\bar{\rho}$.

C. Physical process

The physical process of the RM mixing with reshock is presented in this section. The quantities and the method to calculated them are given as follows:

(i) The evolution of the wave structures (see Fig. 2) is obtained with one-dimensional simulations, in which the computational settings are the same as those in Secs. II A and II B except for an absence of the initial perturbations.

(ii) The growth of the perturbations are shown with the instantaneous field of the gas-1 mass fraction (see Figs. 3 and 4) in the three-dimensional simulations with initial perturbations.

(iii) The energy spectrum of the fluctuating motions (see Fig. 5). The radial density spectra of the cases are given to show the transition process of the turbulent mixing as well as the evolution of different modes [39,63]. The radial spectrum of density is calculated as follows:

$$E_{\rho'}(k, x, t) = \sum_{k-\frac{1}{2} < k_{yz} \leqslant k+\frac{1}{2}} \widehat{\rho'}^* \widehat{\rho'}(x, k_y, k_z, t), \quad (14)$$

with the radial wave number defined as $k_{yz} = \sqrt{k_y^2 + k_z^2}$. $\widehat{\cdot}$ denotes Fourier transform in the y-z plane and $(\cdot)^*$ is its complex conjugate. The spectra are averaged in the central mixing zone defined as the zone with

$$\{x | 4\tilde{Y}_1(x)[1 - \tilde{Y}_1(x)] \geqslant 0.9\}. \quad (15)$$

(iv) In the three-dimensional simulations with initial perturbations, the interface position x_I, or the averaged position of the mixing zone is defined as follows:

$$x_I \equiv \frac{\int_{x_{min}}^{x_{max}} \tilde{Y}_1(1 - \tilde{Y}_1)x dx}{\int_{x_{min}}^{x_{max}} \tilde{Y}_1(1 - \tilde{Y}_1)dx}. \quad (16)$$

The velocity of the interface v_I is the time derivative of x_I [see Figs. 6(a) and 6(d)].

(vi) The growth of the mixing width [see Figs. 6(b) and 6(d)], which is defined as the distance from the bubble-zone front (x_B, the position with a prescribed light-fluid mass fraction $\tilde{Y}_l = 0.05$) to the spike-zone front (x_S, the position with
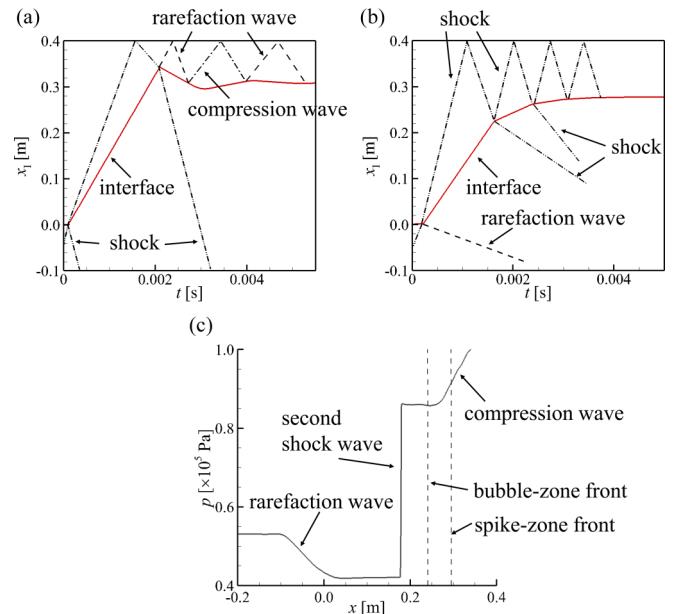
FIG. 2. Displacement of the interface and the wave structures that interact with the interface. The data are obtained with one-dimensional simulations in the cases (a) air-SF$_6$ and (b) SF$_6$-air. In the three-dimensional simulation of the SF$_6$-air case, the distribution of the waves with the aid of the averaged pressure profile at $t = 2.28$ ms is given in panel (c). This shows that in the case of SF$_6$-air, because of the extend of the mixing zone, the third wave is more likely to be a compression wave.

(a) $t = 0.001$ s

(b) $t = 0.002$ s

(c) $t = 0.003$ s

(d) $t = 0.004$ s

(e) $t = 0.001$ s

(f) $t = 0.002$ s

(g) $t = 0.003$ s

(h) $t = 0.004$ s
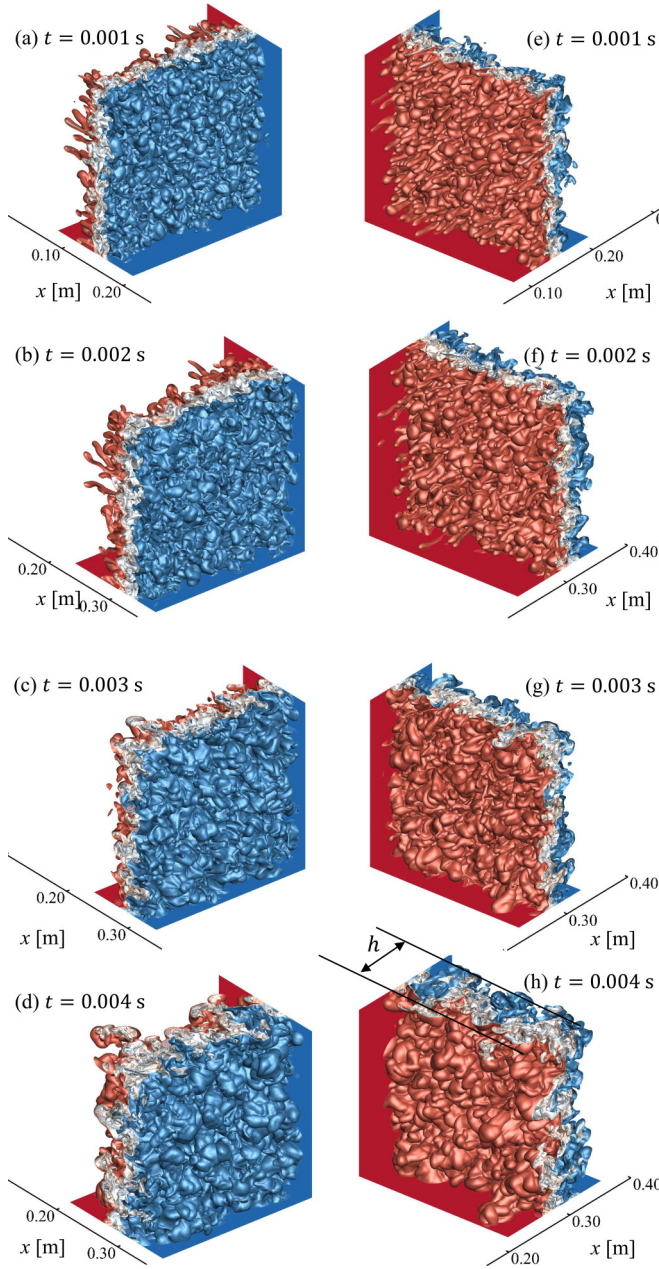
FIG. 3. Instantaneous field of the light-fluid (gas 1) mass fraction in the RM mixing with reshock in the case of air-SF$_6$. The left panels show the evolution of the bubble zone (represented by an isosurface with the mass fraction of gas 1 being 0.1) and the right panels show the evolution of the spike zone (represented by an isosurface with the mass fraction of gas 1 being 0.9). Panels (a), (b), (e), and (f) are before the reshock and panels (c), (d), (g), and (h) are after the reshock.

$\widetilde{Y}_l = 0.95$), i.e.,

$$h \equiv \mathrm{sgn}(A)(x_B - x_S), \qquad (17)$$

where A is the Atwood number. For light-to-heavy cases (the initial shock travels from light gas to the heavy gas), $\mathrm{sgn}(A) = 1$ and $x_B > x_S$. For heavy-to-light cases (the initial shock travels from heavy gas to the light gas), $\mathrm{sgn}(A) < 1$ and $x_B < x_S$.

(a) $t = 0.001$ s

(b) $t = 0.002$ s

(c) $t = 0.003$ s

(d) $t = 0.001$ s

(e) $t = 0.002$ s

(f) $t = 0.003$ s
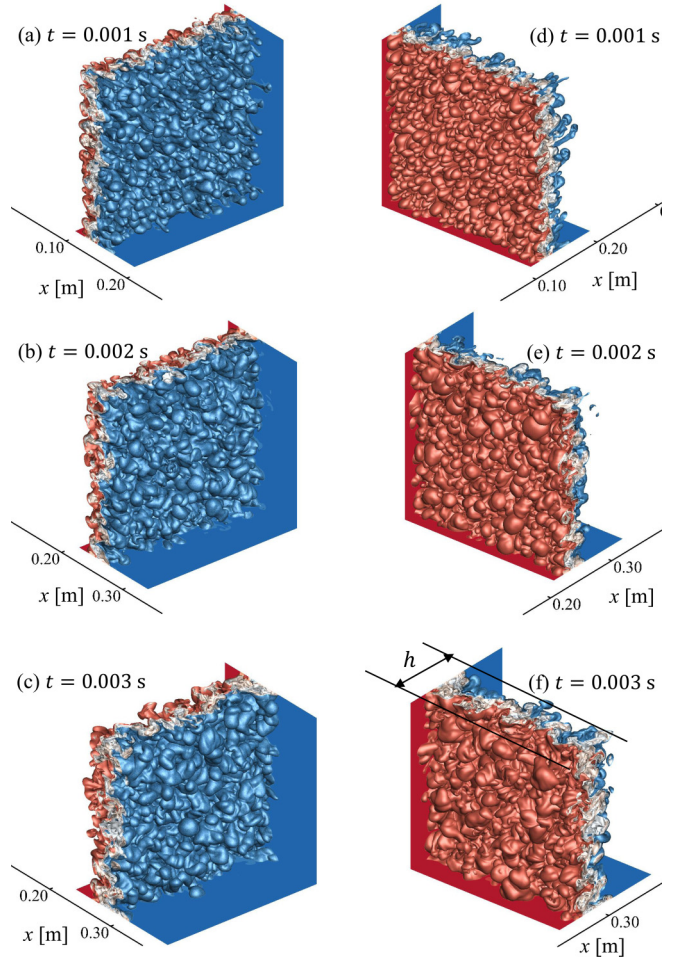
FIG. 4. Instantaneous field of the heavy-fluid (gas 1) mass fraction in the RM mixing with reshock in the case of SF$_6$-air. The left panels show the evolution of the spike zone (represented by an isosurface with the mass fraction of gas 1 being 0.1) and the right panels show the evolution of the bubble zone (represented by an isosurface with the mass fraction of gas 1 being 0.9). Panels (a), (b), (e), and (f) are before the reshock and panels (c), (d), (g), and (h) are after the reshock.

(vii) The molecular mixing fraction, which is used to quantify the amount of the molecularly mixing fluids [64,65]. The molecular mixing fraction [see Figs. 6(c) and 6(f)] is calculated as

$$\Theta = \frac{\int_{x_{\min}}^{x_{\max}} \overline{Y_1 Y_2} dx}{\int_{x_{\min}}^{x_{\max}} \overline{Y_1}\, \overline{Y_2} dx}. \qquad (18)$$

In the light-to-heavy case, the interface is accelerated first by two shock waves and then by the rarefaction wave and compression wave alternatively with their strength decaying. In the heavy-to-light case, the interface is accelerated first by the initial shock wave and then decelerated by several reflected shock waves with decaying strength. In three-dimensional simulations of the heavy-to-light cases, the pressure profiles indicate the waves after the second shock wave are not very sharp [see Fig. 2(c)] and the interface is decelerated gradually [see Fig. 6(d)]. Thus, the waves after the second shock wave are more likely to be compression waves. Therefore,
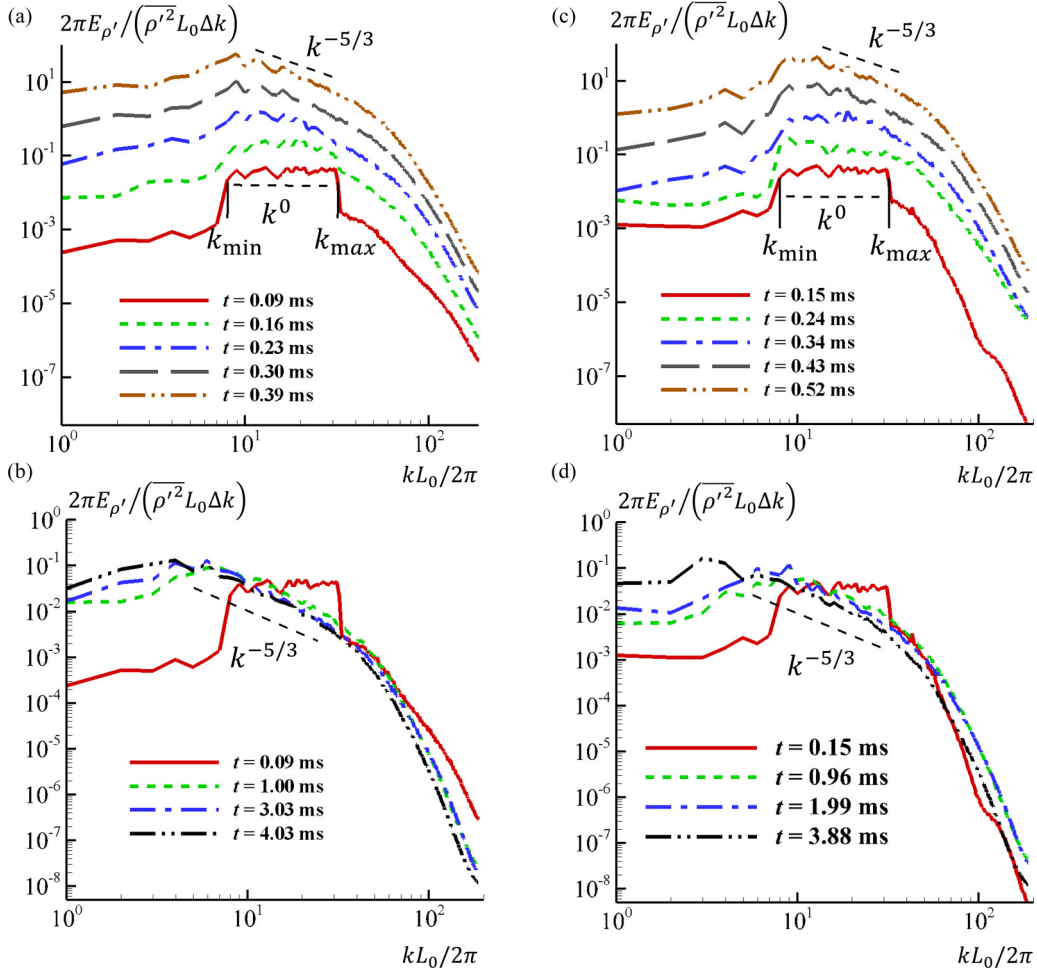
FIG. 5. Evolution of the radial energy spectrum of density for the cases [(a), (b)] air-SF_6 and [(c), (d)] SF_6-air. Panels (a) and (c) show the evolution of energy spectrum during the initial stage after the passage of the first shock wave. Panels (b) and (d) show the evolution of the energy spectrum during the whole process. In panels (a) and (c), the lines are shifted to clarify the profiles. The profile is shifted upward with a value of lg(5) relative to the profile at the previous time sample. $k_{min} = 2\pi/L_{max}$, $k_{max} = 2\pi/L_{min}$, in which L_{min} and L_{max} are defined in Sec. II B. In the vertical axis, $\Delta k = 2\pi/L_0$. The variable is set so that the normalized total energy is 1 when integrated against the horizontal variable.

the waves after the second shock wave will be referred to as compression waves.

Generally, for each case, the whole process is divided into several stages according to the interaction between the mixing zone and the waves. Each period is denoted using the following method: "wave" defines a period when a wave directly interacts with the mixing zone, which is followed by "after wave," defined as the period when the wave leaves the mixing zone. Therefore, the two periods (wave, after wave) makes a couple. For example, (shock 1, after shock 1) denotes the period during the passage of the first shock wave and the period after the passage of the first shock wave. Likewise, in light-to-heavy cases, (shock 2, after shock 2), (rarefaction 1, after rarefaction 1), (compression 1, after compression 1), (rarefaction 2, after rarefaction 2), and (compression 2, after compression 2) are defined; in heavy-to-light cases, (shock 2, after shock 2), (compression 1, after compression 1), and (compression 2, after compression 2) are defined. The periods and the notations used in the paper are listed in Table IV.

Before the shock 2, the flow field is characterized with small-scale bubbles and spikes [Figs. 3(a), 3(b), 3(e), 3(f), 4(a), and 4(d)]. After the shock 2, the scales of the dominate structures grow larger [Figs. 3(c), 3(d), 3(g), 3(h), 4(b), 4(c), 4(e), and 4(f)]. The evolution of each mode is given in Fig. 5. Initially, the energy is constant among the wave numbers ranging from $k_{min} = 2\pi/L_{max}$ to $k_{max} = 2\pi/L_{min}$. As the secondary instability develops, an inertial range with a $k^{-5/3}$ scaling appears, which indicates a transition from nonlinear stage to the turbulent stage of the mixing process. The wave numbers of the lower and upper limits of the inertial range can be denoted with k_l and k_u. When $k_u \geqslant 2k_l$, the energy-containing scales departs from the dissipation scales, and thus mixing transits to turbulence in the mixing zone [66]. By using this criteria, the transition time can be estimated, e.g., $t = 0.39$ ms in the case of air-SF_6 and $t = 0.52$ ms in the case of SF_6-air. Similarly, using the energy spectrum of the density in the cases of air-CO_2 and H_2-air (not shown), the transition time can be approximated as $t = 1.21$ ms and $t = 0.09$ ms, which are marked in Fig. 15. Later on, the energy
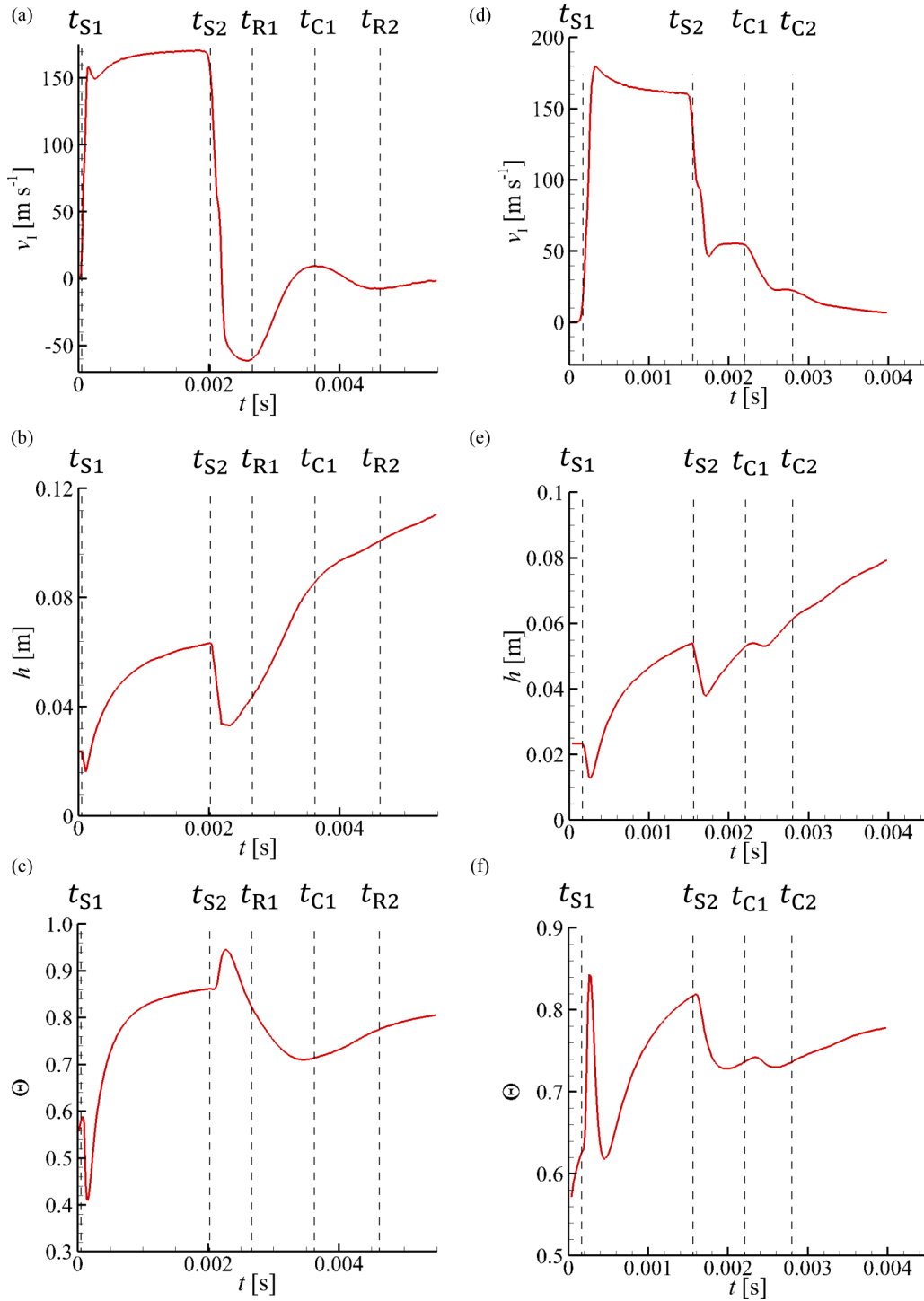
FIG. 6. Evolution of the velocity of the interface v_I [(a), (d)], the mixing width [(b), (e)], and the molecular mixing fraction [(c), (f)]. The results are from the cases of air-SF_6 [(a)–(c)] and SF_6-air [(d)–(f)]. In the case of air-SF_6, the dashed lines mark the time (t_{S1}, t_{S2}, t_{R1}, t_{C1}, t_{R2}) when the waves (the first shock wave, second shock wave, first rarefaction wave, first compression wave, and second rarefaction wave) meet the mixing zone. In the case of SF_6-air, the dashed lines mark the time (t_{S1}, t_{S2}, t_{C1}, and t_{C2}) when the waves (the first shock wave, second shock wave, first compression wave, and second compression wave) meet the mixing zone.

at the smaller wave numbers grow larger [see Figs. 5(b) and 5(d)], indicating the growth of the large-scale structures. The mixing transition corresponds to the rise in the molecular mixing fraction [67]. Figures 6(c) and 6(f) show that after the passage of the first shock wave, the molecular mixing fraction increases quickly, and before reshock, $\Theta = 0.86$ in

the case of air-SF_6 and $\Theta = 0.82$ in the case of SF_6-air, which are approximately the values in the multimode RM mixing at late stage when the mixing approaches the self-similar state, e.g., Refs. [32,42]. When the fluids are well mixed in the small-scale structures, the local Atwood number [42] or the effective Atwood number [67] is small, which will result in a

TABLE IV. The mechanisms controlling the evolution of the mixing width during each period of RM mixing with reshock. NA represents "not applicable." SU represents the "start-up" process. $+$ and $-$ represent positive and negative contributions, respectively.

Cases		Air-CO$_2$		Air-SF$_6$		H$_2$-air		SF$_6$-air	
Periods	Notation	S(C)	Penetration	S(C)	Penetration	S(C)	Penetration	S(C)	Penetration
Shock 1	S1	−	+	−	+	−	+	−	−
After shock 1	AS1	Negligible	+	Negligible	+	Negligible	+	Negligible	+
Shock 2	S2	−	−	−	−	−	−	−	+
After shock 2	AS2	+ in SU	− to +	+ in SU	− to +	+ in SU	− to +	− in SU	+
Rarefaction 1	R1	+	+	+	+	+	+	NA	NA
After rarefaction 1	AR1	Negligible	+	NA	NA	Negligible	+	NA	NA
Compression 1	C1	NA	NA	−	+	−	+	−	+
After compression 1	AC1	NA	NA	NA	NA	NA	NA	Negligible	+
Rarefaction 2	R2	NA	NA	+	+	+	+	NA	NA
Compression 2	C2	NA	NA	NA	NA	−	+	−	+
After compression 2	AC2	NA	NA	NA	NA	Negligible	+	Negligible	+

temporary decrease in the growth rate in RT turbulent mixing and a small growth rate after reshock. This will be discussed in Sec. IV D.

In light-to-heavy cases, after the period shock 1, the interface moves downstream with a quasiconstant velocity. Upon the second shock wave, the interface-velocity reverses. In this stage, the mixing width first decreases and then increases. Later, the mixing zone interacts with rarefaction and compression waves alternatively, while the mixing zone moves toward two directions correspondingly [36,41]. Thus, the mixing zone experiences a variable-acceleration period. In the period of rarefaction 1, the growth rate of mixing width increases significantly, while it slows down substantially in the period of compression 1 [34,36,41] [see Fig. 5(b)]. In heavy-to-light cases, after the period of shock 1, the interface moves downstream. Upon the acceleration of the second shock wave and compression waves, the interface velocity decreases. Influenced by the shock waves and compression waves, the mixing zone is first compressed and then its width increases. It is easy to understand that when the late-stage rarefaction and compression waves meet the mixing zone, the turbulent motions from the previous periods will lead to a continuous increasing in the mixing width, although the corresponding growth rate decays with time, which will be called RM effect hereafter. In the previous research (e.g., Refs. [30,49–51]), it is proposed that the RT effect contributes to the growth of the mixing zone since the mixing is accelerated as a whole object during the rarefaction waves. Similarly, the RT-stable effect also contributes when the heavy fluid accelerates the light fluid [see Fig. 6(a)]. In the next section, a growth-rate-decomposition formula is established, which reveals another mechanism that is very important when the waves interact with the mixing zone, i.e., the S(C) effect induced by the nonuniform velocity distribution in the mixing zone.

III. THE GROWTH-RATE-DECOMPOSITION FORMULA

A. The growth rate of the mixing width

Based on the equation of mixing width [Eq. (17)], its growth rate follows

$$\dot{h} = \text{sgn}(A)(\dot{x}_\text{B} - \dot{x}_\text{S}), \tag{19}$$

i.e., the velocity difference of the bubble-zone front ($\widetilde{Y}_0 = 0.05$) and the spike-zone front ($\widetilde{Y}_0 = 0.95$). The overdot represents a time derivative of the corresponding variable. To understand the speed of the two fronts, one can investigate the speed of a virtual point with a specific mass fraction $\widetilde{Y}_0$, i.e., $\dot{x}_{\widetilde{Y}_0}$. Based on an infinitesimal analysis of the averaged-mass-fraction profile (see Fig. 7 and its caption for details), $\dot{x}_{\widetilde{Y}_0}$ reads

$$\dot{x}_{\widetilde{Y}_0} = -\frac{\partial \widetilde{Y}_1/\partial t}{\partial \widetilde{Y}_1/\partial x}\bigg|_{\widetilde{Y}_0}. \tag{20}$$

Using the equation of the averaged mass fraction

$$\frac{\partial \widetilde{Y}_1}{\partial t} + \widetilde{u}\frac{\partial \widetilde{Y}_1}{\partial x} = \frac{1}{\overline{\rho}}\frac{\partial R_{Y_1 u}}{\partial x} + \frac{1}{\overline{\rho}}\frac{\partial}{\partial x}\left(\overline{\rho D}\frac{\partial \widetilde{Y}_1}{\partial x}\right) + \frac{1}{\overline{\rho}}\frac{\partial}{\partial x}\left(\overline{\rho D \frac{\partial Y_1''}{\partial x}}\right), \tag{21}$$

with the turbulent flux $R_{Y_1 u} \equiv -\overline{\rho Y_1'' u''}$ and D being the mixture diffusion coefficient, one obtains

$$\dot{x}_{\widetilde{Y}_0} = [\overline{u} + V_\text{pen} + V_\text{diff}]\big|_{\widetilde{Y}_0}, \tag{22a}$$

$$V_\text{pen} = \frac{\overline{u'\rho'}}{\overline{\rho}} - \frac{1}{\overline{\rho}}\frac{\partial R_{Y_1 u}/\partial x}{\partial \widetilde{Y}_1/\partial x}, \tag{22b}$$

$$V_\text{diff} = -\frac{1}{\overline{\rho}\partial \widetilde{Y}_1/\partial x}\frac{\partial}{\partial x}\left(\overline{\rho D}\frac{\partial \widetilde{Y}_1}{\partial x} + \overline{\rho D \frac{\partial Y_1''}{\partial x}}\right). \tag{22c}$$

$$\dot{x}_{\widetilde{Y}_0}^* = [\overline{u}^* + V_\text{pen}^* + V_\text{diff}^*]\big|_{\widetilde{Y}_0}, \tag{22d}$$

$$V_\text{pen}^* = \frac{\overline{u'^*\rho'^*}}{\overline{\rho}^*} - \frac{1}{\overline{\rho}^*}\frac{\partial R_{Y_1 u}^*/\partial x^*}{\partial \widetilde{Y}_1/\partial x^*}, \tag{22e}$$

$$V_\text{diff}^* = -\frac{1}{\overline{\rho}^*\partial \widetilde{Y}_1/\partial x^*}\frac{\partial}{\partial x^*}\left(\overline{\frac{1}{\text{ReSc}}\frac{\partial \widetilde{Y}_1}{\partial x^*}} + \overline{\frac{1}{\text{ReSc}}\frac{\partial Y_1''}{\partial x^*}}\right). \tag{22f}$$

In deriving Eq. (22), $\widetilde{u} = \overline{u} + \overline{\rho'u'}/\overline{\rho}$ is applied, where $\overline{u}$ represents the Reynolds-averaged mean velocity. V_pen represents the contribution of fluctuation field and V_diff represents the velocity induced by the diffusive effect. Equations (22d)–(22f) represent the nondimensional form of the growth rate of the mixing width, in which the variables are normalized with
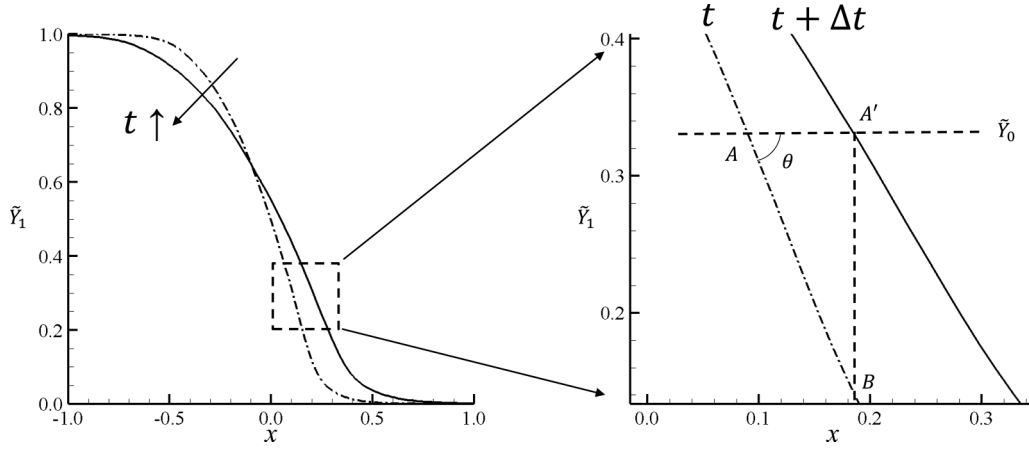
FIG. 7. A scheme showing the evolution of the mass fraction profile to derive the speed of the virtual point with mass fraction of $\widetilde{Y}_0$. At time t, the mass fraction is the dash-dotted line with the virtual point at point A, which changes to the solid line at $t + \Delta t$ with the virtual point denoted with A' (see the right panel). A vertical line starting at A' crosses the profile at time t at point B. The three points A, A', B forms a right triangle. The length $L_{A'B} = \partial \widetilde{Y}_1/\partial t \, \Delta t$. $\tan \theta = -\partial \widetilde{Y}_1/\partial x$. The minus sign is used because $\partial \widetilde{Y}_1/\partial x$ is negative at the sample point. Applying $L_{AA'} = L_{A'B}/\tan \theta$, one gets $\dot{x}_{\widetilde{Y}_0} = \lim_{\Delta t \to 0} L_{AA'}/\Delta t = -(\partial \widetilde{Y}_1/\partial t)/(\partial \widetilde{Y}_1/\partial x)|_{\widetilde{Y}_0}$.

characteristic variables. The characteristic velocity is chosen as the velocity jump of the interface after the passage of the first shock wave, the length scale is chosen as the spanwise length of computational domain and the characteristic density is chosen as the average density of the initial unshocked fluids. Combining the Eqs. (19) and (22), the growth rate of the mixing width is decomposed as

$$\dot{h} = \text{sgn}(A)(\overline{u}|_\text{B} - \overline{u}|_\text{S} + V_\text{pen}|_\text{B} - V_\text{pen}|_\text{S} + V_\text{diff}|_\text{B} - V_\text{diff}|_\text{S}), \tag{23}$$

which will be referred to as the growth-rate-decomposition (GRD) formula.

The turbulent flow in the mixing zone can be decomposed into a mean value and a fluctuating part according to the Reynolds decomposition [52]. For turbulent mixing induced by interfacial instability, the mixing zone grows in the streamwise direction, i.e., the direction of the acceleration in the RT mixing or the velocity of the shock wave in the RM mixing, and the average is performed in the direction along the initially unperturbed interface. From Eq. (23), the growth rate of the mixing width involves contributions of three factors:

(i) The S(C) effect induced by the mean-velocity difference between two ends of the mixing zone. When the mean-velocity difference is not zero, the mixing zone is stretched or compressed.

(ii) The penetration effect induced by the fluctuating velocity. From Eq. (22b), V_pen is determined by the mass flux $\overline{\rho' u'}/\overline{\rho}$, and the gradients of the turbulent flux $R_{Y_1 u}$ and the averaged mass fraction. To be more specific, the mass flux and turbulent flux are dominated by two important processes. The first one is, in light-to-heavy cases, $(Y_1'' > 0, \ u'' > 0)$ or $(\rho' < 0, \ u' > 0)$ and, in heavy-to-light cases, $(Y_1'' < 0, \ u'' < 0)$ or $(\rho' < 0, \ u' < 0)$, which reveals that the light fluid penetrates into the heavy fluid. The second one is, in light-to-heavy cases, $(Y_1'' < 0, \ u'' < 0)$ or $(\rho' > 0, \ u' < 0)$ and, in heavy-to-light cases, $(Y_1'' > 0, \ u'' > 0)$ or $(\rho' > 0, \ u' > 0)$, which reveals that the heavy fluid penetrates into the light fluid. Therefore, the contribution of V_pen difference between

two ends of the mixing zone is named as the penetration effect. This will be analyzed in detail in Sec. III C.

(iii) The diffusive effect, which is induced by the molecular diffusion, because physically it tends to decrease the heterogeneity inherited from the initial separation of two fluids. From Eq. (22f), it is easy to understand that turbulent mixing at high Reynolds number and at Schmidt number of order unity, the diffusive term can be neglected.

It is worth emphasizing that, although the contributions of the mean velocity and the fluctuating part are added independently, they influence each other inherently. For example, when there is a mean velocity gradient in the mixing zone, the turbulent kinetic energy and thus the mass flux $\overline{\rho' u'}/\overline{\rho}$ and the turbulent flux $R_{Y_1 u}$ are enhanced or decreased [41], and thereby the penetration effect is enhanced or decreased correspondingly. Conversely, the turbulent motion decreases the mean velocity gradient according to its averaged equation.

B. The S(C) effect during the propagation of the waves

In this section, the S(C) effect is discussed in detail. When the waves propagate in the mixing zone, a velocity difference between the bubble-zone front and the spike-zone front arises as

$$\Delta V \equiv \text{sgn}(A)(\overline{u}|_\text{B} - \overline{u}|_\text{S}), \tag{24}$$

which stretches or compresses the mixing zone. The origins of the velocity difference during a shock wave and a rarefaction wave are shown in Fig. 8 schematically.

For the shock waves, the two ends of the mixing zone are shocked successively, forming the velocity difference. Since the average density changes in the mixing zone, ΔV changes as well when the shock wave propagates in the mixing zone. When the shock propagates from the heavy fluid to the light fluid, a rarefaction wave forms behind the shock [see Fig. 8(a), left panel]. (For the majority of real gases, the nature of the reflected wave can be identified according to density distribution.) As the shock comes into the mixing zone, the near-wall fluid obtains a velocity jump V_J0 (V_J0 refers to the magnitude of
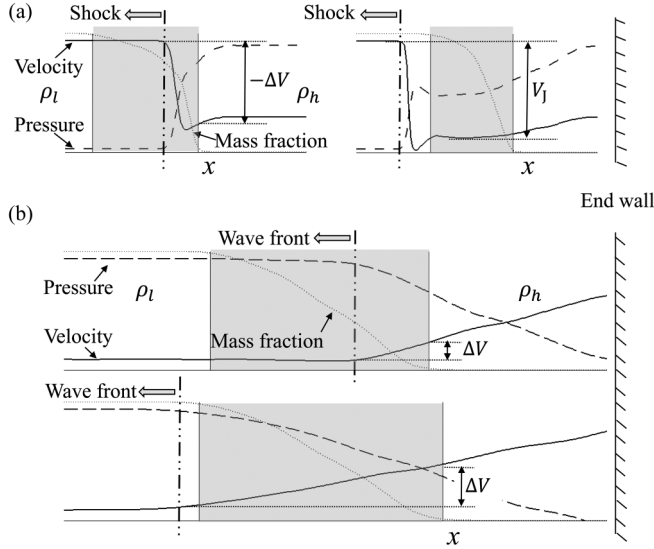
FIG. 8. A scheme to show the origin of the velocity difference during the propagation of the waves in light-to-heavy cases. Variation of extend of the mixing zone (shaded area), mass fraction of the light fluid (dotted line), pressure profile (dashed line), and velocity profile (solid line) when (a) a shock wave and (b) a rarefaction wave passes through the mixing zone. The wavefront lies in the mixing zone [(a) left panel, (b) upper panel] and outside the mixing zone [(a) right panel, (b) lower panel]. Data are taken from the numerical results of the case air-SF$_6$.

FIG. 9. Turbulent statistics from each quadrant normalized by the maximum value for turbulent flux $R_{Y_1 u}$ (left panels) and the mass flux $\overline{\rho' u'}$ (right panels). Panels (a) and (b) are used to define the four events in $R_{Y_1 u}$ and $\overline{\rho' u'}$. Panels (c) and (d) are from the case of air-SF$_6$. Panels (e) and (f) are from the case of SF$_6$-air. The penetration of the light fluid into the heavy fluid is represented by Q1 event in panel (c), by Q2 event in panel (d), and by Q3 event in panels (e) and (f); the penetration of the heavy fluid into the light fluid is represented by Q3 event in panel (c), by Q4 event in panel (d), and by Q1 event in panels (e) and (f).

the velocity jump). Subsequently, as the rarefaction wave accelerates the fluids behind the shock wave, the velocity jump of the near-wall fluid increases. The velocity jump reaches a peak value V_{J1} as the shock arrives at the other end of the mixing zone where V_{J1} is equal to V_J. Therefore, the magnitude of the velocity difference first increases monotonically from V_{J0} to V_J and then decreases to zero as the shock wave leaves the mixing zone (see the period S2 in Figs. 10, 11, and 12 and period S1 in Fig. 13). In contrast, when the shock propagates from the light fluid to the heavy fluid, a compression wave forms behind the shock wave, and velocity difference decreases monotonically from V_{J0} to V_J (see the period S1 in Figs. 10, 11, and 12 and S2 in Fig. 13).

During the propagation of rarefaction and compression waves, as the waves come into the mixing zone from the near-wall side, the fluids occupied by the waves are first accelerated; see Fig. 8(b). Longer periods of accelerations are observed for fluids at shorter distances from the wall. Thus, a velocity gradient arises and the velocity difference emerges correspondingly. When the wavefront arrives at the other end of the mixing zone, the velocity difference reaches its peak value. Then, as the strength of the waves decays, the velocity difference decreases as well, as expected.

C. The penetration effect

From Eq. (22b), $V_{\rm pen}$ is determined by the mass flux $\overline{\rho' u'}/\overline{\rho}$, the gradients of the turbulent flux $R_{Y_1 u}$, and the averaged mass fraction. The relationship between the turbulent statistics and the turbulent structures can be analyzed using the method of

quadrant analysis, which has been successfully used in analyzing the Reynolds shear stress in turbulent channel flow [68].

Using the quadrant analysis, the turbulent flux $R_{Y_1 u}$ can be divided into four categories according to the signs of Y_1'' and u''. Without loss of generality, the light-to-heavy case is used to illustrate this method. The first quadrant (Q1), $Y_1'' > 0$ and $u'' > 0$, indicates the process that the light fluid penetrates into the heavy fluid; the second quadrant (Q2), $Y_1'' < 0$ and $u'' > 0$, contains the motion associated with the heavy fluid flows back to the heavy-fluid side; the third quadrant (Q3), $Y_1'' < 0$ and $u'' < 0$, contains the penetration of the heavy fluid into the light fluid; and the fourth quadrant (Q4), $Y_1'' > 0$ and $u'' < 0$, contains the motion that takes light fluid back to the light-fluid side. Thus, the first- and third-quadrant events contribute to the negative turbulent flux (positive production), and the second- and fourth-quadrant events contribute to the positive turbulent flux (negative production). The contribution to the turbulent flux from each quadrant as a function of x location is shown in Fig. 9(c) at a sample time $t = 3.8$ ms.
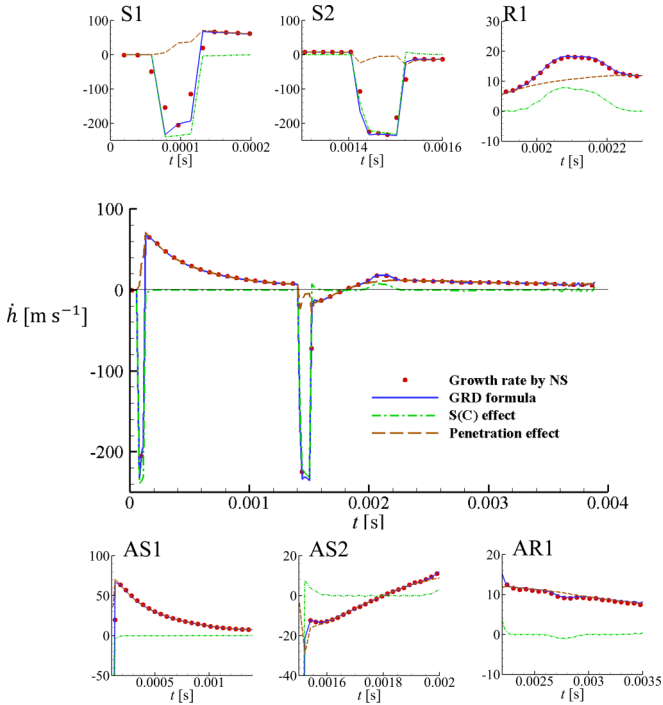
FIG. 10. The evolution of the growth rate by the numerical simulation (NS) (red dotted line) and by the GRD formula (blue lines) as well as the contribution of the S(C) effect (green dash-dotted line) and the penetration effect (brown dashed line) are given. Characteristic periods are isolated to show the contribution of the two effects. The notations of the periods are as follows: S1 for the period of shock 1; AS1 for the period after the shock 1, S2 for the period of shock 2; AS2 for the period after the shock 2; R1 for the period of rarefaction 1 followed by the period AR1. The notations are also listed in Table IV. Data are taken from the case of air-CO_2.

At the spike-zone side, the turbulent flux is dominated by the penetration of the heavy fluid into the light fluid (Q3 event). At the bubble-zone side, the turbulent flux is dominated by the penetration of the light fluid into the heavy fluid (Q1 event). In most parts of the mixing zone, the Q1 and Q3 events dominates the turbulent flux. In the center of the mixing zone (where the turbulent flux is maximum), the turbulent flux from Q1 and Q3 is 1.04 times the total turbulent flux.

Similarly, the turbulent flux in the heavy-to-light cases and the mass flux $\overline{\rho' u'}$ in two configurations can be analyzed. Their results are shown in Fig. 9. A consistent conclusion can be drawn that in the spike-zone side, the turbulent statistics related with species transport are dominated by the penetration of the heavy fluid into the light fluid while in the bubble-zone side, the turbulent statistics are dominated by the penetration of the light fluid into the heavy fluid. In the whole mixing zone, the turbulent statistics are dominated by the penetrations of the two species into each other. Therefore, the contribution of V_{pen} difference between two ends of the mixing zone is named as the penetration effect.

D. The contribution of each mechanism in RM mixing with reshock

The mechanisms controlling the evolution of the mixing width is calculated using GRD formula for the four cases as

shown in Figs. 10–13. The numerical results are a derivative of the mixing width. The two results agree well with each other, which validates the GRD formula [Eq. (23)]. The diffusive effect in Eq. (23) is not involved, which reveals that in the present simulations with high Reynolds numbers, the growth of the mixing width is dominated by large-scale structures and the contribution of the diffusion is negligible. Furthermore, the contribution of the S(C) and the penetration effects are highlighted with enlarged figures. The results are summarized in Table IV, which indicates the following:

(i) During the propagation of shock wave and the compression wave, the mixing zone is compressed, while during the propagation of rarefaction wave, the mixing zone is stretched. After the passage of the shock waves, S(C) effect with small amplitude (relative to the amplitude during the propagations of the waves) is observed, which is negative when the wave travels from the light fluid to the heavy fluid and positive when the wave travels from heavy fluid to light fluid.

(ii) During most duration of the simulation, the penetration effect is positive. One exception is that during the propagation of the shock wave from heavy fluid to the light fluid and a short time after that, the penetration effect is negative, which is consistent with the phase-reversal phenomenon when the shock wave travels from the heavy fluid to the light fluid [69].

(iii) During the propagation of waves, when the light fluid accelerates the heavy fluid (in light-to-heavy cases this corresponds to rarefaction, while in heavy-to-light cases this corresponds to compression waves), the contribution of the penetration effect increases, which is consistent with the RT-instability effect reported in the previous research. Conversely, when the heavy fluid accelerates the light fluid, the penetration effect decreases, which is consistent with the RT-stable effect.

(iv) It is worth noting two complex periods. The first one is during the propagation of shock waves. The second one is the short time after the shock wave leaves the mixing zone, which is called the startup process in the literature [24]. During the propagation of shock waves, both the S(C) and penetration effects contribute to the growth rate. During the startup process, the S(C) effect and the penetration effect are of the same order. However, these two periods have not been well studied yet.

E. The GRD formula and the RM and RT mixing

The GRD formula provides a method to quantitatively analyze the mechanisms controlling the evolution of the mixing width in an interfacial fluid mixing. The growth rate is divided into three parts, i.e., the S(C) effect, the penetration effect, and the diffusive effect. As two special cases of general fluid mixing, the classical RM and RT mixing can be analyzed using the GRD formula.

For the RM instability, it can be analyzed using the processes related with the first shock wave, i.e., shock 1 and after shock 1. During the interaction of the shock wave with the mixing zone, the compression by the mean velocity is significant, which has been reported in the previous research [3]. However, the penetration effect is also important especially when the wave travels from the light fluid to the heavy fluid, which has not drawn enough attention so far. When the shock travels from the heavy fluid to the light fluid, the penetration
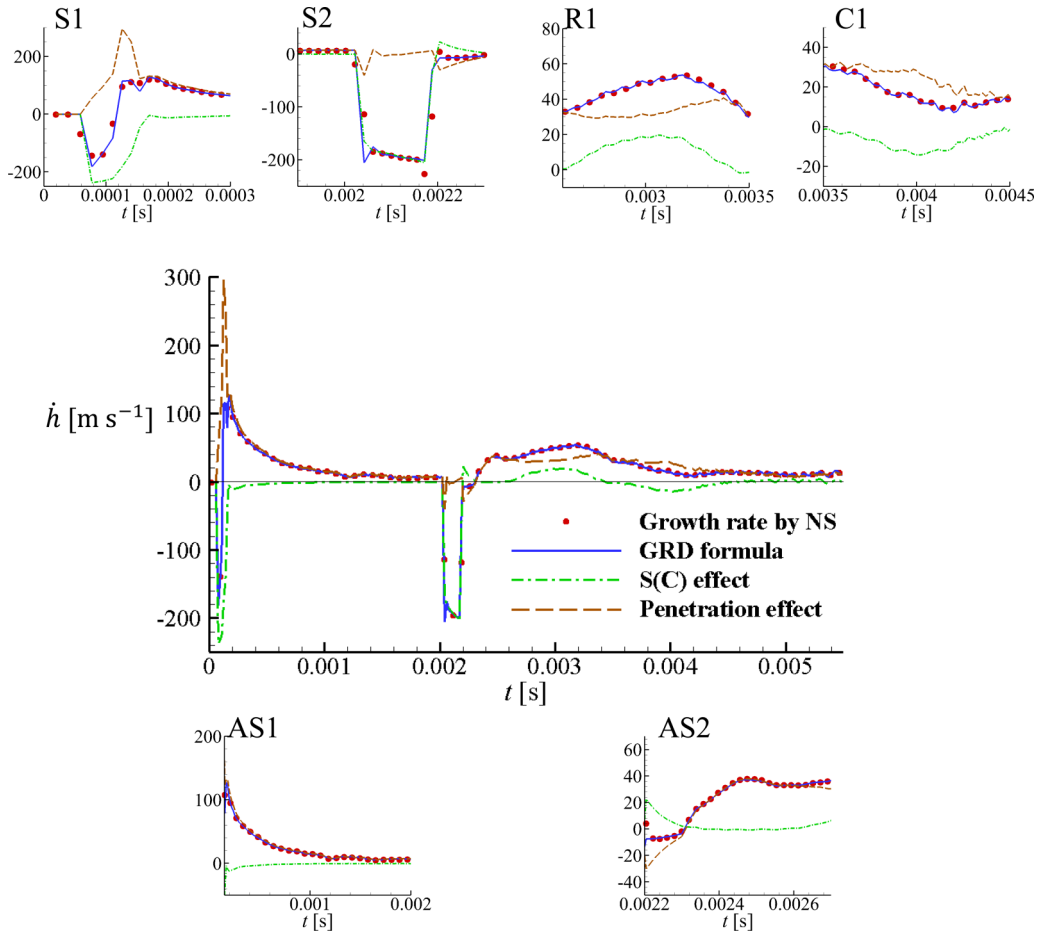
FIG. 11. The evolution of the growth rate by the numerical simulation (NS) (red dotted line) and by the GRD formula (blue lines) as well as the contributions of the S(C) effect (green dash-dotted line) and the penetration effect (brown dashed line) are given. Data are taken from the case of air-SF$_6$. The notations for the periods are given in Table IV.

effect is negative which corresponds to the so-called phase-reversal phenomenon in RM instability. After the shock wave leaves the mixing zone, a startup process is observed, in which the S(C) and penetration effects are both important. Besides, during the startup process, the penetration effect transits from its value during the propagation of the shock waves to the value of the successive linear-growth behavior. Therefore, it is beneficial to divide the classical RM instability into three periods: The first one is the period when the shock wave interacts with the mixing zone, the second one is the startup process, followed by the third period when the penetration effect dominates. It is suggested that the concept of *RM effect* be defined as the interfacial-fluid mixing induced by the initial fluctuation field, e.g., the third period aforementioned.

For the incompressible RT instability, it can be proved that the S(C) effect is zero (see Appendix D for details). For the weak compressible RT instability, the results of a published paper show that the S(C) effect is one order smaller than the penetration effect (see Appendix D for details). When the light fluid accelerates the heavy fluid, the penetration effect increases, which corresponds to a RT-instability effect, while a decrease in penetration effect corresponds to a RT-stable period when the heavy fluid accelerates the light fluid. The *RT effect* thus represents the penetration effect induced by the

external forces (which result in the overall acceleration of the system) during the evolution of the turbulent mixing.

The GRD formula can be used for complex interfacial mixing problems, such as the RM mixing with reshock in the present paper. In the complex problems, it is necessary to emphasize that the S(C) effect is essentially different from the RT effect. Quantitatively, during the early period of the rarefaction and compression waves, the growth rate induced by RT is $2\alpha Agt$ with $\alpha \approx 0.1$ and $A < 1$ while that of the S(C) effect is of ξgt where $\xi \approx O(1)$ (see Appendix E for details). Here g is the acceleration of the system and t starts from the time when the waves meet the mixing zone. This reveals that the growth rate by the S(C) effect is an order larger than that of the RT effect during the propagation of waves. Besides, when the waves interact with the mixing zone, the S(C) effect first increases and then decreases to zero when the waves leave the mixing zone. However, for RT effect, it results in a growth rate that decays slowly after the waves leave the mixing zone (see Figs. 10–13).

From the previous analysis, it is suggested that the penetration effect can be divided into two parts, i.e., the RM effect, which represents the influence of the initial fluctuation field, and the RT effect, which represents the contribution of fluctuation motions induced by the in-process external forces.
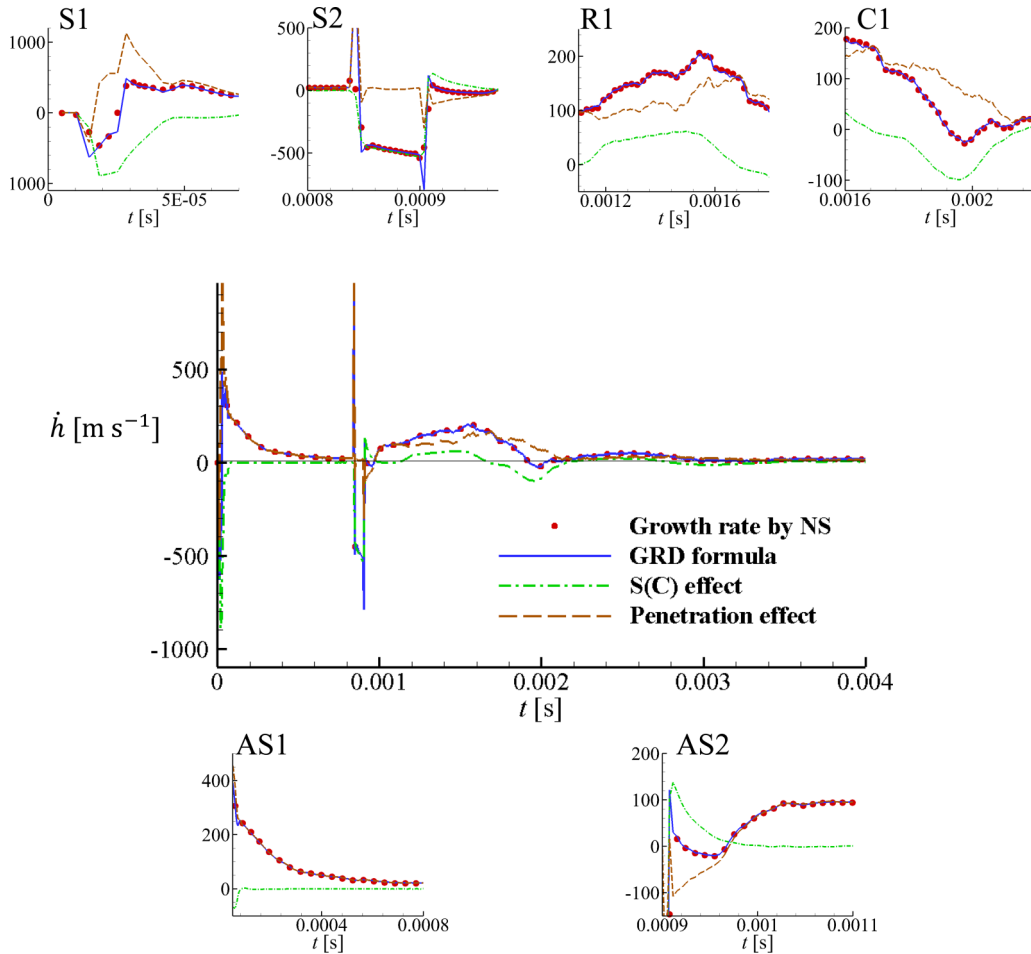
FIG. 12. The evolution of the growth rate by the numerical simulation (NS) (red dotted line) and by the GRD formula (blue lines) as well as the contribution of the S(C) effect (green dash-dotted line) and the penetration effect (brown dashed line) are given. Data are taken from the case of H_2-air. The notations for the periods are given in Table IV.

Therefore, in high-Reynolds-number flow, the three factors, namely S(C), RM, and RT effects control the evolution of the mixing width. This results in the analytical model in the next section, which can describe the complex evolution of the mixing width up to late stage.

IV. ANALYTICAL MODEL FOR THE EVOLUTION OF MIXING WIDTH

In this section, the analytical model for the evolution of the mixing width up to very late stage is proposed. First, the whole process is divided into several stages according to the interaction between the mixing zone and the waves, as described in Sec. II C. In a specific case, some of the periods are too short to identify, and therefore, it is removed from analysis. The resulting periods used in the present cases are summarized in Table IV. Second, for an individual period, the mixing width is described by

$$h_i(t) = h_{i,\mathrm{S(C)}}(t) + h_{i,\mathrm{RM}}(t) + h_{i,\mathrm{RT}}(t), \qquad (25)$$

where h_i denotes the mixing width during the ith stage which starts at $t_{i,0}$. $h_{i,\mathrm{S(C)}}$, $h_{i,\mathrm{RM}}$, and $h_{i,\mathrm{RT}}$ are the contributions of S(C), RM, and RT effects, respectively. Here, it is assumed that the RM and RT effects can be formulated independently.

Equation (25) can be easily reduced to the classical RT and RM instabilities. More importantly, this framework is quite useful for describing the mixing width under successive wave interactions. Note that Eq. (25) is a general framework. One or two terms on the right-hand of Eq. (25) can be zero. For example, in periods after the startup process in AS1 and AS2, the S(C) effect and RT effect are zero and only the RM effect is active. Next, the detailed formulation for each effect are given.

A. S(C) effect

The mixing width induced by the S(C) effect is

$$h_{i,\mathrm{S(C)}}(t) = \int_{t_{i,0}}^{t} \Delta V \, dt. \qquad (26)$$

During the interaction between the waves and the mixing zone, it is approximated that the Reynolds-averaged velocity of different parts of the mixing zone changes with the same trend. This approximation is rational since without the waves, the velocity difference is negligible (in particularly for the Reynolds-averaged velocity); therefore, they should follow a similar routine to change from the initial velocity to the final velocity. This provides a method to estimate the
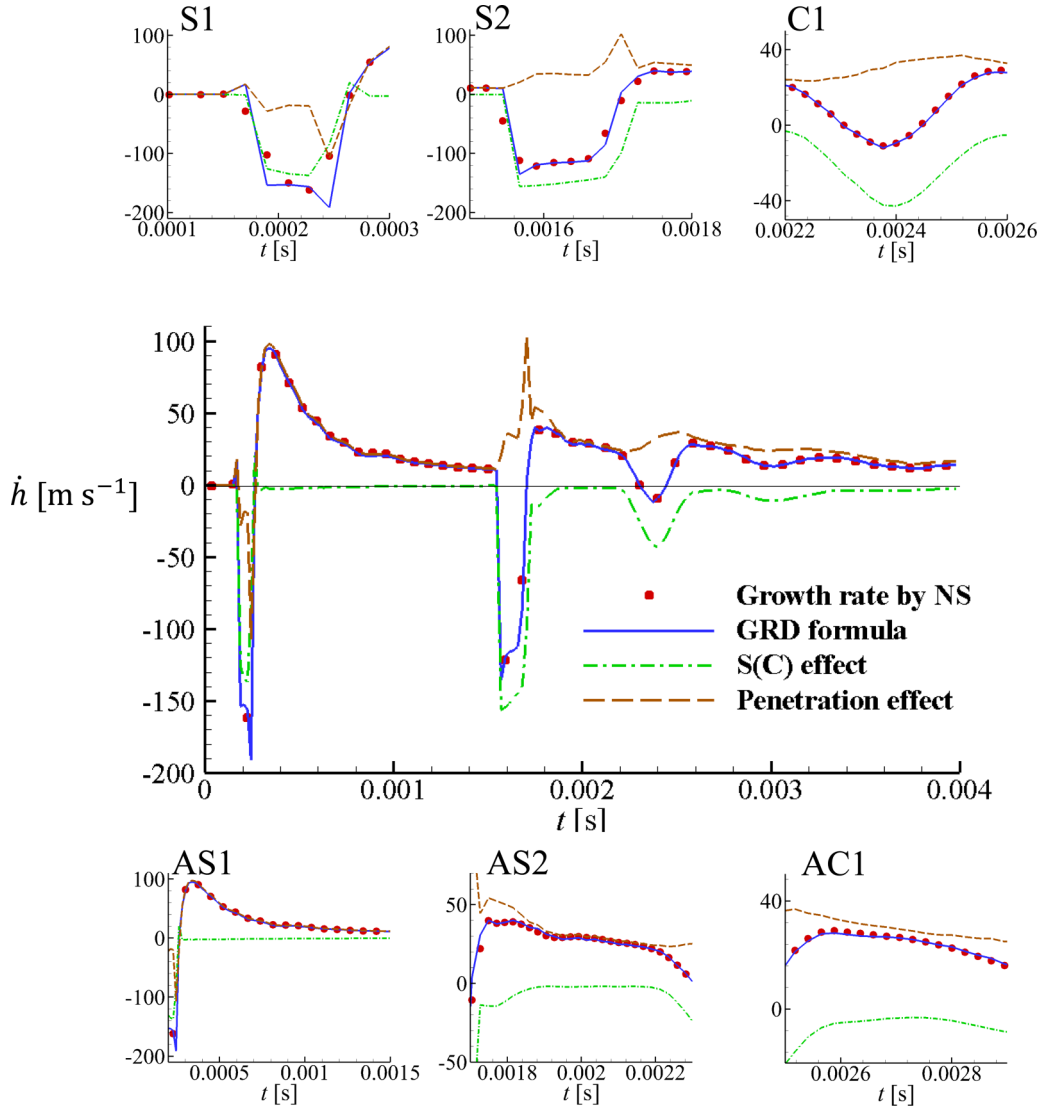
FIG. 13. The evolution of the growth rate by the numerical simulation (NS) (red dotted line) and by the GRD formula (blue lines) as well as the contributions of the S(C) effect (green dash-dotted line) and the penetration effect (brown dashed line) are given. Data are taken from the case of SF_6-air. The notations for the periods are given in Table IV.

velocity at the bubble-zone front $[\overline{u}_B(t)]$ and spike-zone front $[\overline{u}_S(t)]$ by the velocity at the mixing-zone center $[\overline{u}_I(t)]$, i.e., $\overline{u}_S(t) = \overline{u}_I(t - \Delta t_S)$ and $\overline{u}_B(t) = \overline{u}_I(t - \Delta t_B)$, where Δt_S is the difference of the times when the wave front arrives at the mixing-zone center and the spike-zone front while Δt_B is defined similarly for the bubble-zone front. Using Eq. (24), the velocity difference follows

$$\Delta V(t) = \text{sgn}(A)[\overline{u}_I(t - \Delta t_B) - \overline{u}_I(t - \Delta t_S)]. \quad (27)$$

The resulting velocity differences for four cases are shown in Fig. 14, which shows that the velocity difference during the rarefaction and compression waves calculated by the present model agree well with the numerical results. For the velocity difference during the propagation of shock waves, the model obtains values that account for at most 0.79 to 1.29 times of the accurate values that are given by the numerical simulations, suggesting that a further study is needed.

B. RM effect

In the periods AS1 and AS2, after the startup process, the RM effect dominates and a model by combining a linear growth and a power-law growth, which represents a self-similar growth behavior [27,30], is adopted. The linear growth is formulated as

$$h_{i,\text{RM}}(t) = h_{i,0} + 2\alpha_1 A V_J(t - t_{i,0}), \quad (28)$$

and the successive power-law growth is formulated as

$$h_{i,\text{RM}}(t) = h_i^*(1 + (t - t^*)/\tau)^\theta. \quad (29)$$

$h_{i,0}$ is the mixing width at $t_{i,0}$. A is the Atwood number and V_J is the velocity jump because of the shock wave. α_1 is a nondimensional coefficient. The characteristic time $\tau = \theta h_i^*/\dot{h}_i^*$. h_i^* and $\dot{h}_i^*$ are the mixing width and its growth rate (induced by the penetration effect) at the transition time $t^* = \beta h_0/V_J$. h_0 is the mixing width right before the corresponding shock wave.
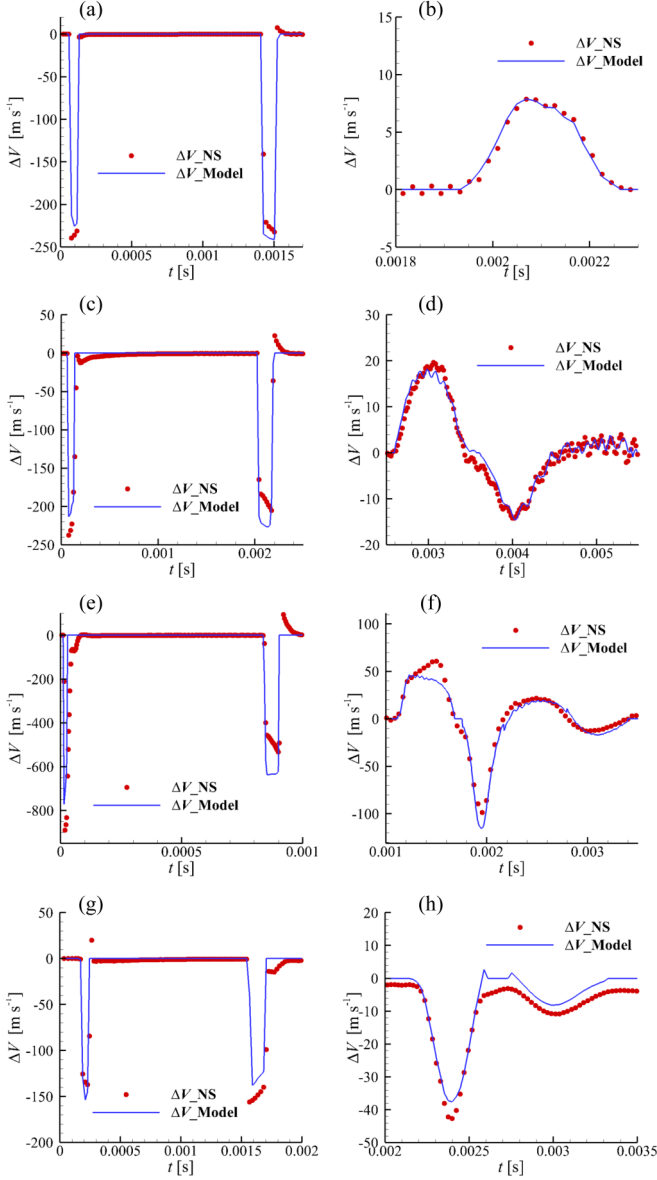
FIG. 14. Velocity difference during the shock waves (left panels), rarefaction, and the compression waves (right panels) calculated by the numerical simulation (NS) (red dotted line) and the present model (27) (blue solid lines). The cases for air-CO_2 [(a), (b)], air-SF_6 [(c), (d)], H_2-air [(e), (f)], and SF_6-air [(g), (h)] are presented.

Equation (29) ensures that the mixing width and growth rate are continuous at t^*.

In the stages during and after the passage of rarefaction and compression waves, it is assumed that the turbulent flow inherited from the earlier stages decays if there is no other energy input, as observed in the late-stage RM mixing. Therefore, this contribution can also be evaluated with the self-similar solution of Eq. (29) by replacing $t^* = t_{i,0}$.

C. RT effect

During the passage of rarefaction and compression waves, the mixing zone is accelerated partially or as a whole object because of the pressure gradient accompanied with the

waves. Precisely speaking, the mixing zone undergoes a variable-acceleration process, i.e., RT mixing under variable acceleration $g(t)$. The width induced by the variable acceleration can be scaled by $\Omega = 0.5(\int \sqrt{g}dt)^2$ or $\Xi = \iint gdt'dt$ [20–22]. For the RT effects induced by the rarefaction or compression waves, the acceleration magnitude first increases and then decreases to zero. Therefore, the length scale Ω is not proper since its growth rate becomes zero immediately when the acceleration is zero, which is obviously not physical. Therefore, the mixing width induced by the RT effects is evaluated with

$$h_{i,\mathrm{RT}}(t) = \alpha_2 A \Xi = \alpha_2 A \int_{t_{i,0}}^{t} \int_{t_{i,0}}^{s} g(t')dt'ds, \qquad (30)$$

where α_2 is a nondimensional parameter and A is the Atwood number. The acceleration is the second derivative of the averaged mixing center [Eq. (16)], i.e., $g(t) = \ddot{x}_\mathrm{I}$. Since x_I is the the averaged center of the mixing zone, $\ddot{x}_\mathrm{I}$ represents an averaged acceleration of the mixing zone so that it can be used for evaluating the mixing width induced by the RT effect.

D. Validations using numerical simulations

To analytically describe the interfacial-fluid mixing process, there are basically two challenges. First, the physical mechanisms determining the evolution of the mixing width should be understood, which has been clarified in the previous sections. Second, the parameters for quantitatively predicting the mixing width corresponding to each mechanism should be specified.

There are two types of input parameters [30]. The first type involves dynamical parameters which vary from case to case, such as the Atwood number, the time when the wave meets the mixing zone, the motion of the mixing zone, etc. Temporarily, one has to rely on numerical simulations or experiments to get the dynamical parameters, e.g., Refs. [30,40,70]. The dynamical parameters are listed in Table V. During the shock-wave stage, the parameter h_0 is the mixing width right before the shock wave. During the propagation of a wave, t_s represents the time when the wave meets the mixing zone, t_{fc} represents the time when the wave front arrives at the center of the mixing zone, and t_{fe} represents the time when the wave front leaves the mixing zone. t_e represents the ending time of the corresponding period. A denotes Atwood number, calculated as $A = (\overline{\rho_\mathrm{B}} - \overline{\rho_\mathrm{S}})/(\overline{\rho_\mathrm{B}} + \overline{\rho_\mathrm{S}})$, where $\overline{\rho_\mathrm{B}}$ and $\overline{\rho_\mathrm{S}}$ are the densities at the bubble-zone front and the spike-zone front, respectively. In the present cases, as the mixing zone moves, the densities of the fluids changes as well. However, the Atwood number does not change significantly as the waves interact with the mixing zone. V_J denotes the velocity jump of the interface because of the shock wave. After the passage of the shock waves, t_{SU} is the time when the startup period ends.

The second type, listed in Table VI, involves the nondimensional parameters. It is now impossible to predict the nondimensional parameters; therefore, some of them are obtained by fitting. For the periods related with the first two shock waves, the nondimensional parameters differ from case to case, and they are obtained by fitting so that the evolution of the mixing width is consistent with the numerical data. In the late stage, when the rarefaction waves and compression waves

TABLE V. Dynamical parameters needed for calculating the mixing width. NA denotes "not applicable". The meaning of the variables can be found in Sec. IV D.

Period	Parameters	Air-CO_2	Air-SF_6	H_2-air	SF_6-air
Shock 1	$h_0[m]$	0.0243	0.0234	0.0212	0.0233
	$10^3 t_s[s]$	0.0584	0.0584	0.0103	0.1700
	$10^3 t_{fc}[s]$	0.0777	0.0773	0.0188	0.2089
	$10^3 t_{fe}[s]$	0.1142	0.1258	0.0255	0.2276
After shock 1	$10^3 t_s[s]$	0.1142	0.1258	0.0255	0.2276
	$10^3 t_{SU}[s]$	0.1480	0.1177	0.0745	0.3011
	$10^3 t_e[s]$	1.4238	2.0423	0.8374	1.5444
	A	0.235	0.652	0.860	−0.635
	$V_J[m\,s^{-1}]$	219.3	171.5	383.0	157.5
Shock 2	$h_0[m]$	0.0454	0.0658	0.0856	0.0541
	$10^3 t_s[s]$	1.4238	2.0423	0.8374	1.5444
	$10^3 t_{fc}[s]$	1.4825	2.1388	0.8783	1.5901
	$10^3 t_{fe}[s]$	1.5216	2.1881	0.8997	1.6830
After shock 2	$10^3 t_s[s]$	1.5216	2.1881	0.8997	1.6830
	$10^3 t_{SU}[s]$	1.9518	2.4810	0.9910	1.8373
	$10^3 t_e[s]$	1.9518	2.6270	1.1199	2.1675
	A	0.232	0.697	0.860	−0.668
	$V_J[m\,s^{-1}]$	241.5	231.0	599.0	109.2
Rarefaction 1	$10^3 t_s[s]$	1.9518	2.6270	1.1199	NA
	$10^3 t_{fc}[s]$	1.9909	2.7310	1.1560	NA
	$10^3 t_{fe}[s]$	2.0105	2.7680	1.1766	NA
	$10^3 t_e[s]$	2.2452	3.6380	1.6767	NA
	A	0.232	0.686	0.849	NA
After rarefaction 1	$10^3 t_s[s]$	2.245	NA	1.6767	NA
	$10^3 t_e[s]$	3.890	NA	1.7592	NA
	A	0.229	NA	0.849	NA
Compression 1	$10^3 t_s[s]$	NA	3.6380	1.7592	2.1675
	$10^3 t_{fc}[s]$	NA	3.8300	1.8671	2.2357
	$10^3 t_{fe}[s]$	NA	3.9150	1.8929	2.3998
	$10^3 t_e[s]$	NA	4.7690	2.1714	2.5885
	A	NA	0.671	0.878	−0.654
After ompression 1	$10^3 t_s[s]$	NA	NA	NA	2.5885
	$10^3 t_e[s]$	NA	NA	NA	2.7532
	A	NA	NA	NA	−0.667
Rarefaction 2	$10^3 t_s[s]$	NA	4.7760	2.1714	NA
	$10^3 t_{fc}[s]$	NA	4.8360	2.2230	NA
	$10^3 t_{fe}[s]$	NA	5.0000	2.2746	NA
	$10^3 t_e[s]$	NA	5.5000	2.7955	NA
	A	NA	0.668	0.866	NA
Compression 2	$10^3 t_s[s]$	NA	NA	2.7955	2.7531
	$10^3 t_{fc}[s]$	NA	NA	2.8832	2.8238
	$10^3 t_{fe}[s]$	NA	NA	2.9657	2.9898
	$10^3 t_e[s]$	NA	NA	3.3938	3.3260
	A	NA	NA	0.866	−0.676
After compression 2	$10^3 t_s[s]$	NA	NA	3.3938	3.3260
	$10^3 t_e[s]$	NA	NA	4.0000	3.9551
	A	NA	NA	0.866	−0.674

come into effect, the mixing is in the turbulent regime and similar coefficients among different cases can be expected. Therefore, the parameters for the rarefaction 1 period in the case of air-SF_6 are first obtained by fitting and then they are used for the successive periods and the corresponding periods in other light-to-heavy cases. Similarly, the parameters for the compression1 period in the case of SF_6-air are obtained by fitting and then they are used for the successive periods in the case of SF_6-air.

After the passage of the shock wave, β is used to calculate the duration of the linear-growth stage, i.e., $t^* = \beta h_0/V_J$. In the present cases, $\beta = 1.9$ is used for three light-to-heavy cases and $\beta = 0.9$ is used for the heavy-to-light case. α_1 is used to calculate the linear growth rate after the passage of the shock wave, i.e., $\dot{h} = 2\alpha_1 A V_J$. Results show that α_1 changes from case to case and the values after the second shock wave are generally smaller than that after the first shock wave. This is because of the large molecular mixing fraction before

TABLE VI. Nondimensional parameters needed for calculating the mixing width.

Period	Parameters	Air-CO_2	Air-SF_6	H_2-air	SF_6-air
After shock 1	β	1.90	1.90	1.90	0.90
	α_1	0.50	0.34	0.30	0.45
	θ	0.25	0.20	0.20	0.28
After shock 2	β	1.90	1.90	1.90	0.90
	α_1	0.08	0.12	0.08	0.20
	θ	0.28	0.20	0.20	0.28
Rarefaction 1	θ	0.28	0.28	0.28	NA
	α_2	0.45	0.45	0.45	NA
After rarefaction 1	θ	0.28	NA	0.28	NA
Compression 1	θ	NA	0.28	0.28	0.38
	α_2	NA	0.45	0.45	0.45
After compression 1	θ	NA	NA	NA	0.38
Rarefaction 2	θ	NA	0.28	0.28	NA
	α_2	NA	0.45	0.45	NA
Compression 2	θ	NA	NA	0.28	0.38
	α_2	NA	NA	0.45	0.45
After compression 2	θ	NA	NA	0.28	0.38

reshock [see Figs. 6(c) and 6(f)], which can lead to a small growth rate of mixing width after reshock [42]. θ is the power index to calculate the mixing width in the late-stage RM effect. For the light-to-heavy cases, θ varies from 0.20 to 0.28, which is similar to the value that Thornber *et al.* [32] obtains with narrow-band initial perturbations. For the heavy-to-light case, $\theta = 0.38$, higher than those of the light-to-heavy cases. α_2 is used to calculate the RT effect [Eq. (30)] during the passage of rarefaction and compression waves. $\alpha_2 = 0.45$ is used for all the related periods in the four cases. It is noted that the coefficients given in Table VI are not general since the coefficients used for different effects depends on the initial conditions [13,14,16–18,32].

The mixing width obtained by numerical simulations and those obtained with the models considering different factors are shown in Fig. 15 for the four cases. For the period when the shock waves interact with the mixing zone and the startup period after it, there is no widely accepted model; therefore, the mixing width by numerical simulation is adopted. In particular, the S(C) effects are evaluated both by the present model in Sec. IV A and by the numerical simulations, and the resulting mixing width turn out to agree well with each other. After the startup process, the RM effect dominates, and therefore, the profiles considering the RM effect describes the evolution of mixing width very well, which is consistent with the previous research [30]; however, it deviates from the numerical results significantly in the late stage after reshock. When the RT effect is involved, the growth rate increases during the propagations of first rarefaction wave and decreases during the compression waves in light-to-heavy cases while in the heavy-to-light cases the growth rate increases during the propagation of compression waves. The results are further improved and are in very good agreement with the numerical results when the S(C) effect during the rarefaction and compression waves is considered. Thus, the combined effects of S(C) and RT explain the complex evolution of growth rate in the late stage. These facts indicate that the factors considered in Eq. (25) are physical and that the quantitative model can capture these factors well.

It is noted that the present model can be used to describe the evolution of the mixing width rather than to predict it. The dynamical parameters can mostly be obtained from one-dimensional simulations. However, the nondimensional parameters depend initial perturbations, especially during the early-stage evolution. In applications, the model can be used to estimate the magnitude of the mixing width. To enhance the applicability of the model, more systematical work needs to be done to determine the dependence of the nondimensional parameters on the initial perturbations.

V. SUMMARY

Based on decomposing the turbulent flow into the averaged field and the fluctuating counterpart, a GRD formula is established, which shows that the growth of the turbulent-mixing width is controlled by the S(C) effect, the penetration effect, and the diffusive effect. The diffusive effect is negligible for the turbulent mixing with high Reynolds number at Schimdt number of order unity. The penetration effect is further divided into the RM and RT effects which represent the influence of the initial fluctuations and the fluctuations that arise (or decrease) when the mixing zone is subjected to external forces. The model of RM mixing with reshock is used to illustrate these effects. Results show that when the waves interact with the mixing zone, the S(C) effect is significant. To be specific, during the propagation of shock wave and the compression waves, the mixing zone is compressed while during the propagation of rarefaction waves the mixing zone is stretched. After the startup period following the shock waves, the growth rate is dominated by the RM effect. During the passage of rarefaction and compression waves, the S(C), RM, and RT effects are all important. Accordingly, an analytical model is proposed for the evolution of the mixing width up to the very late stage when the strength of the waves is negligible. The results obtained for four typical cases with different light- and heavy-gas combinations indicate that the model can be applied to problems with a wide range of density ratios.
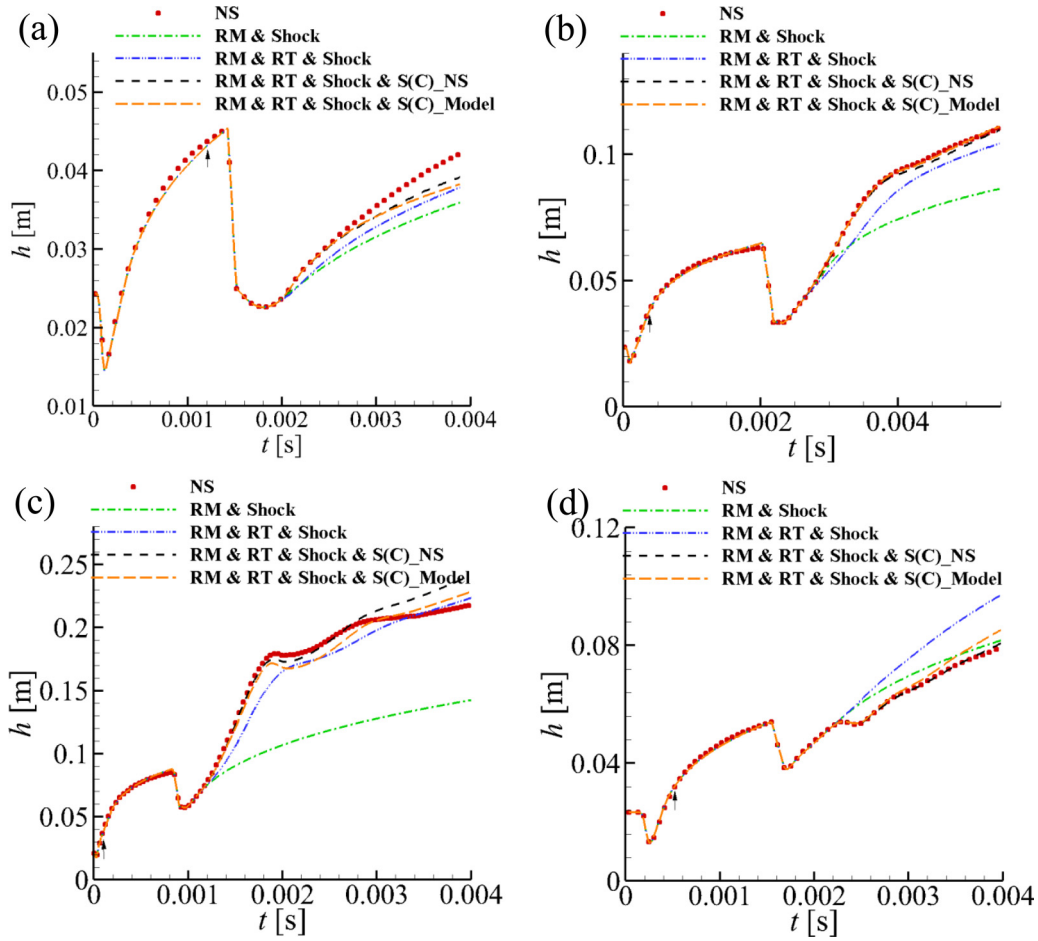
FIG. 15. Mixing width obtained by the numerical simulations (NSs) and by the models considering some of the factors in Eq. (25). "RM" and "RT" represent the RM and RT effects, respectively. "Shock" represents the mixing width during the shock waves, which is obtained from the numerical results. "S(C)" denotes the S(C) effect during rarefaction and compression waves, with the suffix "_NS" indicating the velocity difference calculated from the NS and "_Model" indicating that the velocity difference is calculated from the model [Eq. (27)]. The four cases of air-CO_2 (a), air-SF_6(b), H_2-air (c), and SF_6-air (d) are presented. The black arrows mark the transition time as described in Sec. II C.

The present work also highlights the complexity of mixing process when the shock wave interacts with the mixing zone and during the startup period. During the propagation of shock waves, the penetration effect is also important. For example, when the shock wave travels from the light fluid to the heavy fluid, the growth rate induced by the penetration effect can be of the same order with that of the S(C) effect (e.g., periods S1 in Figs. 10–12 and S2 in Fig. 13). Besides, the numerical results show that after the shock waves leave the mixing zone, the S(C) effect is not zero. When the shock travels from the light fluid to the heavy fluid it is negative, while it is positive when the shock wave travels from the heavy fluid to the light fluid, which makes the startup process even more complex. Therefore, further investigation should be carried out on the modeling of the S(C) and penetration effects during the propagation of shock waves and in the startup process.

The present work provides a GRD formula to quantitatively analyze the growth mechanism in complex interfacial fluid mixing. In the future, it will be applied to fluid mixing under convergent geometries, which has practical meanings for the natural phenomenon and for the engineering applications.

APPENDIX A: SPECIFICATION OF THE INITIAL PERTURBATIONS

The perturbations at the surface satisfy a power spectrum given as

$$P(k) = \begin{cases} Ck^\xi & k_{\min} < k < k_{\max} \\ 0 & \text{otherwise} \end{cases}, \tag{A1}$$

where $k = \sqrt{k_y^2 + k_z^2}$ denotes the one-dimensional wave number of perturbations. The root mean square of the

perturbations (σ) is prescribed, i.e., $\int_{k_{\min}}^{k_{\max}} P(k)dk = \sigma^2$. In this way, the constant C is determined.

In two-dimensional wave space, the amplitude of the mode (k_m, k_n) satisfies

$$a(k_m, k_n) \sim \sqrt{\frac{P(k_{mn})}{2\pi k_{mn}}}, \qquad (A2)$$

where $k_{mn} = \sqrt{k_m^2 + k_n^2}$. In physical space, the perturbations are of the form

$$\begin{aligned}
\eta(y, z) = \sum_{m,n} &a_{mn}\cos(k_m y)\cos(k_n z) \\
&+ b_{mn}\sin(k_m y)\cos(k_n z) \\
&+ c_{mn}\cos(k_m y)\sin(k_n z) \\
&+ d_{mn}\sin(k_m y)\sin(k_n z), \qquad (A3)
\end{aligned}$$

where $k_{m(n)} = m(n)k_0$ and $k_0 = 2\pi/L_0$. The amplitude coefficients a_{mn}, b_{mn}, c_{mn}, and d_{mn} are random numbers chosen from a Gaussian distribution so that the standard deviation is proportional to $\sigma_{mn} = \sqrt{P(k_{mn})/(2\pi k_{mn})\Delta k_m \Delta k_n}$. Here $\Delta k_m = \Delta k_n = k_0$. The relevant demonstration on the transformation from the wave space [Eq. (A1)] to the physical space [Eq. (A3)] has been given by Ref. [32].

In the present work, the power index $\zeta = 0$, $k_{\min} = 2\pi/L_{\max}$, and $k_{\max} = 2\pi/L_{\min}$, where $L_{\max} = L_0/8$ and $L_{\min} = L_0/32$. The root mean square of the perturbations σ equals $\lambda_{\min}$. Thus, the average value of the coefficients follows

$$\overline{a_{mn}} = \overline{b_{mn}} = \overline{c_{mn}} = \overline{d_{mn}} \qquad (A4)$$

$$= \frac{1}{\sqrt{3}\pi}\sqrt{\frac{\lambda_{\min}^3 k_0^2}{k}}. \qquad (A5)$$

The parameters chosen are used so that the perturbations can develop into turbulence soon after the first shock wave.

APPENDIX B: VALIDATION WITH THE θ-GROUP CASE

The original θ-group case [31] is a benchmark case designed to compare eight independent codes. This simulation is initialized with narrow-band perturbations. The initial length scales of the perturbations range from $L/8$ to $L/4$, with L being the length of the cross section of the computational domain. The energy of the initial modes are constant, resulting in a root mean square of the amplitude being $0.1\lambda_{\min}$. The density ratio of the heavy and light fluid is 3:1 and the adiabatic index $\gamma = 5/3$ for both gases. The initial shock wave travels from the heavy fluid to the light fluid. A premix width $\delta = L/32$ is used. For the basic quantities describing the mixing process, such as mixing width, the results have converged with 256 grid nodes in the spanwise direction. Therefore, in the present work, a numerical simulation is carried out using a grid resolution of $364 \times 256 \times 256$ in a domain of $1.4L \times L \times L$. The mixing width is obtained by integrating the averaged mole-fraction profile, i.e., $W = \int_0^{L_x} \overline{X_l}(1 - \overline{X_l})dx$. Figure 16 shows that the present mixing width agrees well with the the code-averaged mixing width in Ref. [31], which validates the present code as well as the method to generate the initial perturbations.
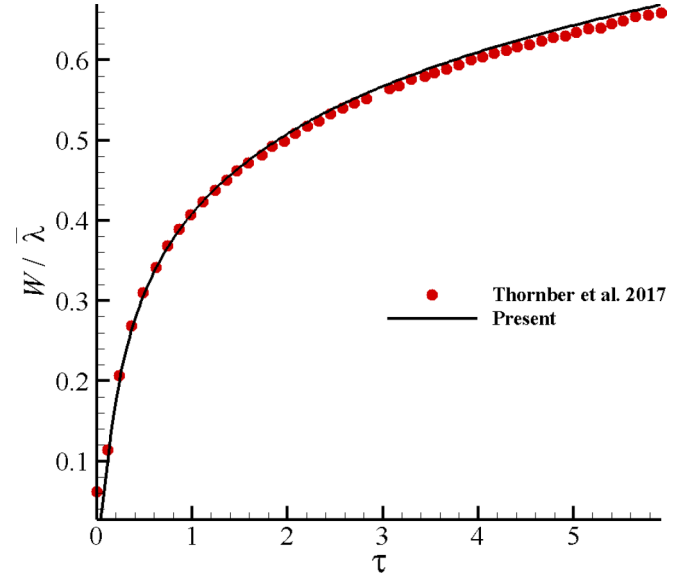
FIG. 16. The evolution of nondimensional mixing width as a function of the nondimensional time obtained by the present code and from the code-averaged mixing width in Ref. [31].

APPENDIX C: GRID-CONVERGENCE STUDY

The case of air-SF$_6$ is simulated with four sets of grid numbers to test the influence of the grid resolution on the primary results. Rectangle grid elements are used. The cases have grid numbers of $280 \times 125 \times 125$, $640 \times 250 \times 250$, $960 \times 375 \times 375$, and $1280 \times 500 \times 500$, which are named cases G125, G250, G375, and G500 respectively. The evolutions of the bubble-zone front, the interface, and the spike-zone front are shown in Fig. 17(a) and the evolution of the mixing width is shown in Fig. 17(b). Results show that the two finest grid cases give approximately the same profiles, indicating that they have converged. Therefore, the grid resolution with 375 grids nodes in 0.2 m is applied in the simulations.

APPENDIX D: THE MEAN-VELOCITY DIFFERENCE IN RT INSTABILITY

It is proved that the velocity difference between two ends of the mixing zone is zero in incompressible RT instability
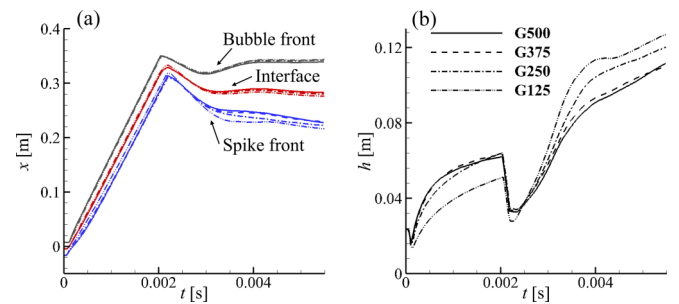
FIG. 17. A grid-convergence study for the air-SF$_6$ case. The evolutions of the bubble-zone front, interface, and spike-zone front are shown in panel (a). The evolution of the mixing width is shown in panel (b).
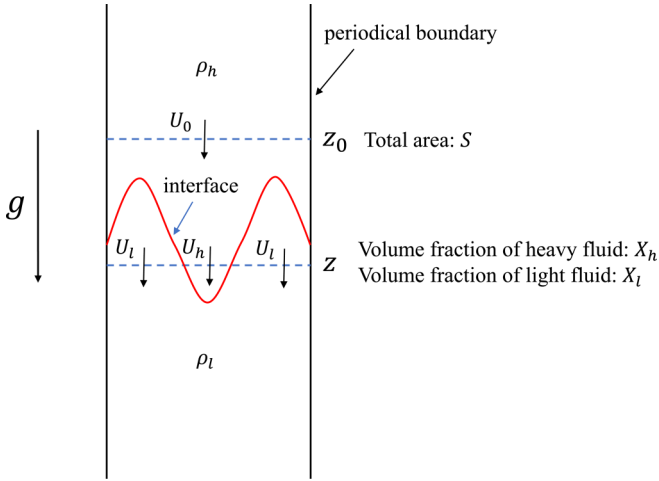
FIG. 18. The Reynolds-averaged velocity in classical-incompressible RT instability. In this configuration, two fluids, with ρ_h being the density of the heavy fluid and ρ_l being the density of the light fluid, are put in a gravitational fluid $\vec{g}$. The interface is denoted with a red line. The area of the cross section is S. The mean velocity at z_0 is U_0. At an arbitrary position z, the mean velocity and volume fraction of the heavy and light fluids are X_h, U_h and X_l, U_l, respectively. Since the fluids are incompressible, the volume of the fluid flowing into the frame across z_0 is $U_0 S \Delta t$, while that flowing out from z is $U_h S X_h \Delta t + U_l S X_l \Delta t$. The volume enclosed by z and z_0 is constant; therefore, $U_0 S = U_h S X_h + U_l S X_l$. The Reynolds-averaged mean velocity ar z is defined as $U_z \equiv (U_h S X_h + U_l S X_l)/S$. Therefore, $U_z = U_0$. In this way, it is proved that the Reynolds-averaged mean velocity is U_0 everywhere in the z direction.

and is much smaller than the growth rate induced by the penetration effect in weak compressible RT instability. For classical RT instability, it refers to a configuration in which the heavy fluid is supported by the light fluid in a gravitational field or two superposed fluids are accelerated. The

fluids are assumed to be incompressible. In this situation, it can be proved that the Reynolds-averaged velocity is uniform in the vertical direction (see Fig. 18). For compressible RT instability, the averaged velocity is assumed to be zero in theoretical analysis [71]; i.e., there is no velocity difference between two ends of the mixing zone. To find out the influence of the compressibility on the averaged velocity, the numerical simulation of a compressible RT instability [72] is reanalyzed (the original data are provided by the authors of Lai *et al.* [72]). This is a RT-instability problem of a compressible flow simulated with a discrete Boltzmann model [73,74]. The initial interface is cosine shaped and the instability is influenced both by thermodynamic and hydrodynamic nonequilibrium effects. The compressibility can be measured by the Mach number. Using the characteristic velocity of single-mode RT instability $v \sim \sqrt{g/k}$, where g is the acceleration and k is the wave number, and the sound speed $c \equiv \sqrt{dp/d\rho}$, the Mach number is approximately 0.17 [72]. Therefore, this case corresponds to the weak compressibility regime. The instantaneous fields of density, vertical velocity, and the Reynolds-averaged velocity are shown in Fig. 19. This indicates that, in the weak compressibility regime, the variation in the Reynolds-averaged velocity is one order smaller than the velocity of the bubble and the spike. Therefore, it is reasonable to neglect the mean-velocity gradient in analytical models [71].

APPENDIX E: AN ANALYSIS OF VELOCITY DIFFERENCE ON DIMENSIONAL GROUNDS

The velocity difference during the propagation of rarefaction and compression waves can be obtained by analyzing this problem on dimensional grounds. When the wave front lies in the mixing zone, the characteristic physical variables are the acceleration of the interface $\ddot{x}_I$, the density ratio, the length occupied by the waves Δx, and the velocity of the wave front V_w. A velocity scale is deduced as $\ddot{x}_I \Delta x / V_w$, and a
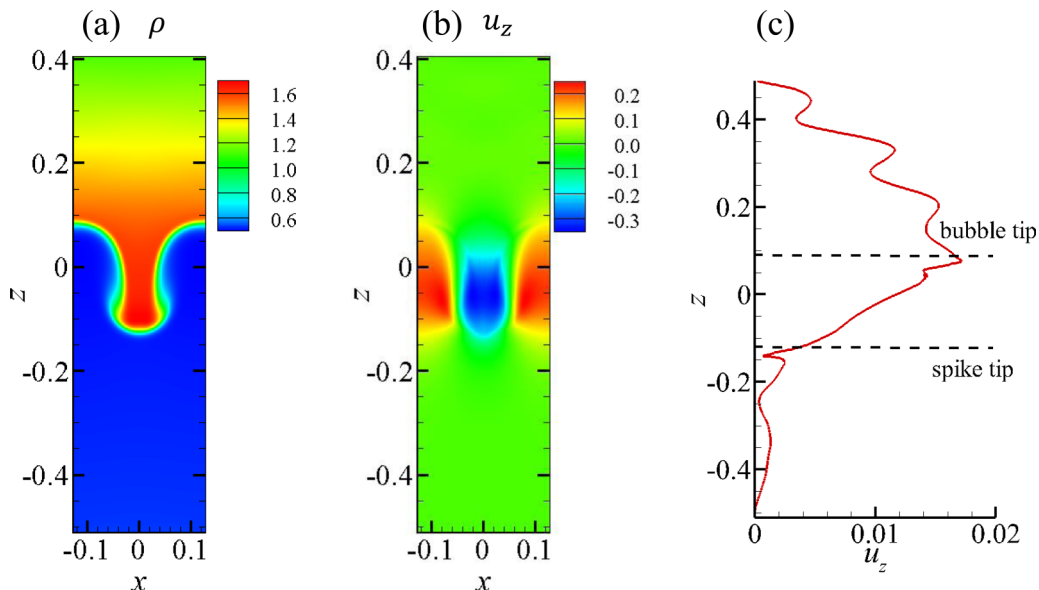
FIG. 19. Instantaneous field of density (a), vertical velocity (b), and the plane-averaged vertical velocity (c). These are results of a compressible RT-instability case and the data are from the authors of Ref. [72].

coefficient that includes the influence of the density ratio ξ can be introduced. By approximating $\Delta x/V_w$ with Δt (the time interval that starts when the wave front meets the mixing-zone edge), one obtains $\Delta V = \xi \ddot{x}_I \Delta t$, where ξ is a nondimensional velocity difference.

According to the analysis in Sec. IV A, before the wave front arrives at the other end of the mixing zone,

$\Delta V \approx \Delta V_B$ in light-to-heavy cases, i.e., the velocity increase at the near-wall side of the mixing zone. Since the velocity at different parts of the mixing zone accelerates with the same trend, $\ddot{x}_B(t) \approx \ddot{x}_I(t - \Delta t_B)$. Therefore, $\xi = \Delta V/(\Delta t \ddot{x}_I) \approx \Delta V_B/(\Delta t \ddot{x}_I) = \ddot{x}_B/\ddot{x} \approx 1$. The same analysis can be performed in heavy-to-light cases. Therefore, $\xi \sim O(1)$.

[1] L. Rayleigh, *Scientific Papers* (Cambridge University Press, Cambridge, UK, 1900), Vol. II.

[2] G. Taylor, Math. Phys. Eng. Sci. **201**, 192 (1950).

[3] R. D. Richtmyer, Commun. Pure Appl. Math. **XIII**, 297 (1960).

[4] E. E. Meshkov, Fluid Dyn. **4**, 101 (1969).

[5] Y. S. Zhang, Z. W. He, F. J. Gao, X. L. Li, and B. L. Tian, Phys. Rev. E **93**, 063102 (2016).

[6] V. A. Thomas and R. J. Kares, Phys. Rev. Lett. **109**, 075004 (2012).

[7] R. Betti and O. A. Hurricane, Nat. Phys. **12**, 435 (2016).

[8] A. Burrows, Nature (London) **403**, 727 (2000).

[9] H. Kull, Phys. Rep. **206**, 197 (1991).

[10] N. Inogamov, Astrophys. Space Phys. **10**, 1 (1999).

[11] Y. Zhou, Phys. Rep. **723**, 1 (2017).

[12] N. A. Inogamov, Pisma Zh. Tekh. Fiz. **4**, 743 (1978).

[13] N. A. Inogamov, A. M. Oparin, A. Y. Dem'yanov, L. N. Dembitskǐ, and V. A. Khokhlov, J. Exp. Theor. Phys. **92**, 715 (2001).

[14] G. Dimonte, Phys. Rev. E **69**, 056305 (2004).

[15] G. Dimonte, D. L. Youngs, A. Dimits, S. Weber, and M. Marinak, Phys. Fluids **16**, 1668 (2004).

[16] G. Dimonte, P. Ramaprabhu, D. L. Youngs, M. J. Andrews, and R. Rosner, Phys. Plasmas **12**, 056301 (2005).

[17] D. L. Youngs, Philos. Trans. R. Soc. A **371**, 20120173 (2013).

[18] D. L. Youngs, Phys. Scr. **92**, 074006 (2017).

[19] B. Akula and D. Ranjan, J. Fluid Mech. **795**, 313 (2016).

[20] G. Dimonte and M. Schneider, Phys. Rev. E **54**, 3740 (1996).

[21] K. O. Mikaelian, Phys. Rev. E **89**, 053009 (2014).

[22] P. Ramaprabhu, V. Karkhanis, R. Banerjee, H. Varshochi, M. Khan, and A. G. W. Lawrie, Phys. Rev. E **93**, 013118 (2016).

[23] M. Brouillette, Annu. Rev. Fluid Mech. **34**, 445 (2002).

[24] M. Lombardini and D. I. Pullin, Phys. Fluids **21**, 044104 (2009).

[25] J. W. Grove, R. Holmes, D. H. Sharp, Y. Yang, and Q. Zhang, Phys. Rev. Lett. **71**, 3473 (1993).

[26] U. Alon, J. Hecht, D. Mukamel, and D. Shvarts, Phys. Rev. Lett. **72**, 2867 (1994).

[27] U. Alon, J. Hecht, D. Ofer, and D. Shvarts, Phys. Rev. Lett. **74**, 534 (1995).

[28] N. A. Inogamov, JETP Lett. **75**, 547 (2002).

[29] N. A. Inogamov and A. M. Oparin, arXiv:physics/0503190v1.

[30] K. O. Mikaelian, Shock Waves **25**, 35 (2015).

[31] B. Thornber, J. Griffond, O. Poujade, N. Attal, H. Varshochi, P. Bigdelou, P. Ramaprabhu, B. Olson, J. Greenough, Y. Zhou, O. Schilling, K. A. Garside, R. J. R. Williams, C. A. Batha, P. A. Kuchugov, M. E. Ladonkina, V. F. Tishkin, N. V. Zmitrenko, V. B. Rozanov, and D. L. Youngs, Phys. Fluids **29**, 105107 (2017).

[32] B. Thornber, D. Drikakis, D. L. Youngs, and R. J. R. Williams, J. Fluid Mech. **654**, 99 (2010).

[33] M. Vetter and B. Sturtevant, Shock Waves **4**, 247 (1995).

[34] D. J. Hill, C. Pantano, and D. I. Pullin, J. Fluid Mech. **557**, 29 (2006).

[35] E. Leinov, G. Malamud, Y. Elbaz, L. A. Levin, G. Ben-Dor, D. Shvarts, and O. Sadot, J. Fluid Mech. **626**, 449 (2009).

[36] M. Lombardini, D. J. Hill, D. I. Pullin, and D. I. Meiron, J. Fluid Mech. **670**, 439 (2011).

[37] F. F. Grinstein, A. A. Gowardhan, and J. R. Ristorcelli, Philos. Trans. R. Soc. A **371**, 20120217 (2013).

[38] J. W. Jacobs, V. V. Krivets, V. Tsiklashvili, and O. A. Likhachev, Shock Waves **23**, 407 (2013).

[39] V. K. Tritschler, B. J. Olson, S. K. Lele, S. Hickel, X. Y. Hu, and N. A. Adams, J. Fluid Mech. **755**, 429 (2014).

[40] J. Ding, T. Si, J. Yang, X. Lu, Z. Zhai, and X. Luo, Phys. Rev. Lett. **119**, 014501 (2017).

[41] H. Li, Z. He, Y. Zhang, and B. Tian, Phys. Fluids **31**, 054102 (2019).

[42] B. Thornber, D. Drikakis, D. L. Youngs, and R. J. R. Williams, Phys. Fluids **23**, 095107 (2011).

[43] D. K. Ilnitsky, K. E. Gorodnichev, A. A. Serezhkin, S. E. Kuratov, N. A. Inogamov, and E. E. Gorodnichev, Phys. Scr. **94**, 074003 (2019).

[44] K. Gorodnichev, P. Zakharov, S. Kuratov, I. Menshov, and E. Gorodnichev, Phys. Fluids **32**, 034101 (2020).

[45] G. Bouzgarrou, Y. Bury, S. Jamme, L. Joly, and J. F. Haas, J. Fluids Eng. **136**, 091209 (2014).

[46] K. O. Mikaelian, Phys. D (Amsterdam, Neth.) **36**, 343 (1989).

[47] F. Poggi, M. H. Thorembey, and G. Rodriguez, Phys. Fluids **10**, 2698 (1998).

[48] C. Mügler and S. Gauthier, Phys. Fluids **12**, 1783 (2000).

[49] R. V. Morgan, O. A. Likhachev, and J. W. Jacobs, J. Fluid Mech. **791**, 34 (2016).

[50] R. V. Morgan, W. H. Cabot, J. Greenough, and J. W. Jacobs, J. Fluid Mech. **838**, 320 (2018).

[51] Y. Liang, Z. Z. Zhai, X. S. Luo, and C. Y. Wen, J. Fluid Mech. **885**, A42 (2020).

[52] O. Reynolds, Philos. Trans. R. Soc. London A **186**, 123 (1895).

[53] D. C. Wilcox, *Turbulence Modeling for CFD* (DCW Industries, La Canada, CA, 2006), p. 515.

[54] S. J. Reckinger, D. Livescu, and O. V. Vasilyev, J. Comput. Phys. **313**, 181 (2016).

[55] W. Sutherland, Philos. Mag. Edinb. **5**, 507 (1893).

[56] Z. R. Zhou, Y. S. Zhang, and B. L. Tian, Phys. Rev. E **97**, 033108 (2018).

[57] Z.-X. Hu, Y.-S. Zhang, B. Tian, L. He, and Z. Li, Phys. Fluids **31**, 104108 (2019).

[58] Z.-X. Hu, Y.-S. Zhang, and B.-L. Tian, Phys. Rev. E **101**, 043115 (2020).

[59] M. J. Xiao, Y. S. Zhang, and B. L. Tian, Phys. Fluids **32**, 032107 (2020).

[60] Z. W. He, Y. S. Zhang, F. J. Gao, X. L. Li, and B. L. Tian, Comput. Fluids **140**, 1 (2016).

[61] F. J. Gao, Y. S. Zhang, Z. W. He, and B. L. Tian, Phys. Fluids **28**, 114101 (2016).

[62] F. J. Gao, Y. S. Zhang, Z. W. He, L. Li, and B. L. Tian, AIP Adv. **7**, 075020 (2017).

[63] H. Liu and Z. Xiao, Phys. Rev. E **93**, 053112 (2016).

[64] D. L. Youngs, Phys. Fluids **3**, 1312 (1991).

[65] D. L. Youngs, Laser Part. Beams 725 (1994).

[66] Y. Zhou, Plasma Phys. **14**, 082701 (2006).

[67] A. W. Cook, W. Cabot, and P. L. Miller, J. Fluid Mech. **511**, 333 (2004).

[68] J. Kim, P. Moin, and R. Moser, J. Fluid Mech. **177**, 133 (1987).

[69] G. Jourdan and L. Houas, Phys. Rev. Lett. **95**, 204502 (2005).

[70] M. El Rafei, M. Flaig, D. L. Youngs, and B. Thornber, Phys. Fluids **31**, 114101 (2019).

[71] D. Livescu, Phys. Fluids **16**, 118 (2004).

[72] H. Lai, A. Xu, G. Zhang, Y. Gan, Y. Ying, and S. Succi, Phys. Rev. E **94**, 023106 (2016).

[73] D. Li, H. Lai, A. Xu, G. Zhang, C. Lin, and Y. Gan, Acta Phys. Sin. **67**, 080501 (2018).

[74] H. Ye, H. Lai, D. Li, Y. Gan, C. Lin, L. Chen, and A. Xu, Entropy **22**, 500 (2020).